RNA reinforces condensate nucleation on chromatin to amplify oncogenic transcription

Krista A. Budinich[1,2,3,4#], Xinyi Yao[5#], Chujie Gong[1,2,3,4#], Lele Song[1,2,4], Michelle C. Lee[1,2,4,6], Qinglan Li[1,2,4], Sylvia Tang[1,2,4], Kaeli M. Mathias[1,2,4,7,8], Yiman Liu[1,2,4], Son C. Nguyen[4,9], Eric F. Joyce[4,9], Yuanyuan Li[5*], Haitao Li[5,10,11*], and Liling Wan[1,2,4,12,13*]

[1]Department of Cancer Biology, University of Pennsylvania, Philadelphia, PA, 19104, USA.

[2]Abramson Family Cancer Research Institute, Perelman School of Medicine, University of Pennsylvania, Philadelphia, PA, 19104, USA.

[3]Cell and Molecular Biology Graduate Group, Perelman School of Medicine, University of Pennsylvania, Philadelphia, PA 19104, USA.

[4]Penn Epigenetics Institute, University of Pennsylvania, Philadelphia, PA, 19104, USA.

[5]State Key Laboratory of Molecular Oncology, MOE Key Laboratory of Protein Sciences, Beijing Frontier Research Center for Biological Structure, School of Basic Medical Sciences, Tsinghua University, Beijing 100084, China.

[6]School of Arts and Sciences, University of Pennsylvania, Philadelphia, PA, 19104, USA.

[7]Biochemistry and Molecular Biophysics Graduate Group, Perelman School of Medicine, University of Pennsylvania, Philadelphia, PA, 19104, USA.

[8]Center for Computational and Genomic Medicine, The Children's Hospital of Philadelphia, Philadelphia, PA, 19104, USA.

[9]Department of Genetics, Perelman School of Medicine, University of Pennsylvania, Philadelphia, PA, 19104, USA.

[10]Tsinghua-Peking Center for Life Sciences, Beijing 100084, China.

[11]SXMU-TM Collaborative Innovation Center for Frontier Medicine, Shanxi Medical University, Taiyuan 030001, China.

[12]Institute for Regenerative Medicine, Perelman School of Medicine, University of Pennsylvania, Philadelphia, PA, 19104, USA.

[13]Lead contact

[#] These authors contributed equally.

[*]Correspondence should be addressed to L.W. (liling.wan@pennmedicine.upenn.edu), H.L. (lht@tsinghua.edu.cn), Y. Li (liyuanyuan@tsinghua.edu.cn)

ABSTRACT

Aberrant chromatin-associated condensates have emerged as drivers of transcriptional dysregulation in cancer, yet the mechanisms regulating their formation and function remain poorly understood. Gain-of-function mutations in the histone acetylation reader ENL, found in leukemia and Wilms tumor, drive oncogenesis by inducing condensate formation at highly selective genomic loci. Here, we uncover a critical role for RNA in reinforcing the nucleation, chromatin engagement, and oncogenic activity of ENL mutant condensates. Mutant ENL binds RNA via a conserved basic patch within its YEATS domain, and this interaction enhances condensate formation both *in vitro* and across diverse cellular contexts. Using a chemically inducible condensate displacement and re-nucleation system, we show that blocking ENL–RNA interactions or transcription impairs condensate reformation at endogenous targets. RNA interactions preferentially enhance ENL occupancy at condensate-permissive loci, leading to increased transcriptional bursting and robust gene activation at the single-cell and single-allele level. In mouse models, disrupting ENL–RNA interactions diminishes condensate formation and oncogenic transcription in hematopoietic stem and progenitor cells, thereby suppressing ENL mutation-driven leukemogenesis. Together, these findings establish RNA as an active cofactor that pathogenic condensates exploit to reinforce locus-specific nucleation and amplify transcriptional programs that drive disease.

16 **INTRODUCTION**

17 An increasing number of chromatin-associated proteins have been shown to form nuclear
18 condensates—high local-concentration assemblies often driven by dynamic multivalent interactions[1]. In
19 some cases, these condensates enrich transcriptional machinery at specific genomic loci to regulate
20 gene expression[2-8]. Dysregulation of condensate formation has been implicated in a range of diseases,
21 notably cancer[9-11]. Genetic mutations or chromosomal translocations in regulatory proteins can induce
22 aberrant condensates, which may be co-opted by cancer cells to activate and sustain oncogenic gene
23 programs[9-11]. However, the molecular mechanisms that regulate the assembly and function of pathogenic
24 condensates remain poorly understood.

25 RNA has long been recognized as a key component of various biomolecular condensates,
26 including stress granules, the nucleolus, and nuclear speckles[12-14]. Emerging evidence suggests that
27 RNA can also modulate condensates formed by transcriptional regulators. For instance, RNA has been
28 proposed to regulate transcription through a feedback mechanism: low levels of RNA produced during
29 transcription initiation promote condensate formation, while elevated RNA levels accumulated during
30 elongation stimulate their dissolution[15]. In pluripotent stem cells, RNA transcribed from endogenous
31 retroviral elements has been shown to facilitate the hijacking of super-enhancer-associated
32 condensates[16]. Despite these advances, whether and how RNA regulates the formation and function of
33 chromatin-associated pathogenic condensates remains largely unexplored.

34 To address this question, we leverage oncogenic ENL (Eleven-nineteen-leukemia) mutants found
35 in pediatric acute myeloid leukemia (AML) and Wilms tumor[17-21]. In its wildtype form, ENL binds
36 acetylated histones via its YEATS domain and promotes transcriptional elongation at target genes[22,23].
37 We previously demonstrated that cancer-associated hotspot mutations in the ENL YEATS domain induce
38 aberrant condensate formation at selective target loci, such as the *HOXA* cluster. These condensates are
39 required for ENL mutation-induced chromatin occupancy, hyperactivation of target genes, and
40 tumorigenesis[24-26]. However, how these condensates are regulated remains unknown. Given the role of
41 RNA in other nuclear condensates[12] and emerging evidence that many transcriptional regulators interact
42 with RNA[27-32], we hypothesized that RNA may modulate ENL mutant condensates. The robust

43 condensate-forming ability, high locus specificity, and potent oncogenic activity of ENL mutants make
44 them an ideal model for dissecting the regulatory mechanisms of pathogenic condensates.
45 Here, we uncover a positive role for RNA in promoting ENL mutant condensate formation and
46 function. ENL mutants bind RNA via a conserved basic patch within the YEATS domain, and this
47 interaction enhances condensate nucleation and transcriptional bursting at permissive loci. Disrupting
48 ENL:RNA interactions impairs oncogenic gene activation and tumorigenesis in mouse models. These
49 findings reveal an RNA-dependent mechanism regulating pathogenic condensates and establish RNA as
50 a functional co-factor in condensate-mediated gene dysregulation in cancer.
51
52 **RESULTS**
53 **ENL binds RNA via a conserved basic patch in the YEATS domain *in vitro* and in cells**
54 A previous study showed that AF9, a paralog of ENL, can bind DNA in part through residues in its YEATS
55 domain[33]. To assess whether ENL shares this property, we performed electrophoretic mobility shift assay
56 (EMSA) using purified full-length wildtype ENL (ENL-WT) and the oncogenic ENL-T1 mutant, the most
57 common of eight patient-derived hotspot mutations found within ENL's YEATS domain (Fig. 1a). We
58 found that ENL-WT bound double-stranded DNA (dsDNA) in a concentration-dependent manner, and the
59 T1 mutation did not alter this capacity (Extended Data Fig. 1a, b).
60 To test whether ENL can also bind RNA, we performed EMSA with a single-stranded nascent
61 RNA (ssRNA) fragment derived from *HOXA11*—a known ENL-T1 target gene whose nascent transcripts
62 are detected within cellular ENL-T1 condensates[25]—and found that ENL-WT and T1 bound *HOXA11*
63 RNA with comparable affinities (Extended Data Fig. 1c,d). These results indicate that ENL harbors RNA-
64 binding capacity and this capability is preserved in cancer-associated ENL mutants. Given the strong
65 enrichment of nascent RNA in ENL-T1 condensates[25] and the reported role of RNA in modulating
66 transcriptional condensates[15], we focused our study on the role of ENL:RNA interactions in condensate
67 formation and function.
68 We next sought to identify the region within ENL that mediates RNA interaction. Given that AF9
69 binds DNA through its YEATS domain, we examined the electrostatic surface potential of ENL's YEATS

70 domain and identified four positively charged surface patches that could engage with negatively charged
71 RNA (Fig. 1b). To evaluate RNA-binding propensity, we modeled interactions between the ENL YEATS
72 domain and ~100 diverse RNA sequences using AlphaFold3 (Extended Data Fig. 1e and Supplementary
73 Table 1). This analysis highlighted the basic patch encompassing residues K61-K67 as the region most
74 likely to interact with RNA (Fig. 1c). Notably, several positively charged residues within this region align
75 with the DNA-binding residues identified in AF9 (Extended Data Fig. 1f). Structural inspection revealed
76 that among these residues, K61, R63, and K67 are surface-exposed and accessible, whereas R64 is
77 less exposed (Extended Data Fig. 1g).

78 To test the contribution of this region to RNA binding, we generated a charge-neutralizing triple
79 alanine mutant (K61A/R63A/K67A, hereafter '3A') predicted to preserve the overall YEATS domain
80 structure (Extended Data Fig. 1h). AlphaFold3 modeling showed that the T1-3A mutant exhibited
81 significantly fewer predicted contacts with RNA compared to T1, suggesting a potential role for these
82 residues in RNA interaction (Fig. 1d and Extended Data Fig. 1i). EMSA using full-length proteins and a
83 nascent *HOXA11* RNA fragment confirmed that T1-3A exhibited reduced RNA binding relative to T1,
84 while retaining partial interactions likely mediated by other basic regions outside of the YEATS domain
85 (Fig. 1e, f). EMSA using purified YEATS domains alone showed that the 3A mutation markedly impaired
86 RNA binding (Extended Data Fig. 1j, k), validating this basic patch as the key RNA-binding surface within
87 the YEATS domain.

88 To determine whether ENL binds RNA in cells, we performed CLAP-seq (Covalent Linkage and
89 Affinity Purification followed by sequencing), an adaptation of CLIP-seq optimized to more directly detect
90 protein–RNA interactions under denaturing conditions[34]. We expressed Halo-tagged ENL-WT, T1, or T1-
91 3A at near endogenous levels in HEK293 cells (Extended Data Fig. 2a), UV-crosslinked protein–RNA
92 complexes, affinity-purified ENL and its associated RNAs using Halo ligand resin under denaturing
93 conditions, and sequenced the recovered RNAs (Fig. 1g). Comparison of CLAP pull-downs with matched
94 inputs identified ~1,600 RNA peaks across all three genotypes, with fewer than 10% unique to any single
95 condition (Extended Data Fig. 2b and Supplementary Table 2). Biological replicates were highly
96 correlated (Extended Data Fig. 2c). WT and T1 displayed similar CLAP signal intensities across the

97 merged peak set (Fig. 1h), consistent with their comparable RNA-binding capacity observed by EMSA
98 (Extended Data Fig. 1c, d). T1-3A bound largely to these same peak regions, but with reduced signal
99 (Fig. 1h, i). These results established that ENL binds RNA in cells and that this interaction is in part
100 mediated by the K61/R63/K67 basic patch.

101 Genomic analysis revealed that the majority of CLAP input peaks mapped to exonic regions,
102 reflecting the high abundance of spliced mRNA in the cell (Fig. 1j and Extended Data Fig. 2d). In
103 contrast, ENL CLAP peaks were strongly enriched in intronic regions (Fig. 1j and Extended Data Fig. 2e),
104 suggesting that ENL primarily binds nascent transcripts. Annotation of CLAP peaks to genes revealed
105 that ENL-bound RNAs were predominantly protein-coding (Fig. 1k and Extended Data Fig. 1f), consistent
106 with ENL's known localization to protein-coding genes[22,26] (Fig. 1k). When plotting CLAP signal across
107 the gene bodies of these targets, we found that ENL-WT and T1 exhibited similar levels of RNA
108 association, with T1 showing a modest increase. In contrast, T1-3A showed reduced RNA association
109 across these gene bodies (Fig. 1l-n, Extended Data Fig. 2g, and Supplementary Table 3).

110 Altogether, our *in vitro* and cellular findings demonstrate that ENL binds RNA and that this
111 interaction depends, at least in part, on a conserved basic patch within its YEATS domain. We therefore
112 adopted ENL-T1-3A as a molecular tool to probe how partially impaired ENL:RNA interactions affect the
113 formation and function of condensates driven by cancer-associated mutations.

114

115 **RNA enhances droplet formation of oncogenic ENL mutant *in vitro***

116 To test whether RNA contributes to ENL condensate formation, we performed *in vitro* droplet
117 assays using purified full-length ENL and RNA, including total RNA extracted from whole cells or nuclear
118 fractions, as well as with chemically synthesized nascent RNA from *HOXA11*, a known ENL-T1 target
119 gene (Fig. 2a-c and Extended Data Fig. 3a-d). ENL-T1 formed droplets more readily than WT in the
120 absence of RNA, consistent with increased self-association conferred by the oncogenic mutation[25].
121 Addition of RNA enhanced droplet formation of both ENL-WT and T1 in a dose-dependent manner, with
122 T1 showing a more pronounced increase (Fig. 2b, c and Extended Data Fig. 3a-d).

123 To determine whether this RNA responsiveness depends on the basic patch in the YEATS
124 domain, we tested the T1-3A mutant. Notably, the 3A mutation did not impair the intrinsic droplet forming
125 abilities conferred by the T1 mutation, as observed in the absence of RNA (Fig. 2b, c and Extended Data
126 Fig. 3a-d). Rather, 3A specifically impaired RNA-dependent enhanced droplet formation (Fig. 2b, c and
127 Extended Data Fig. 3a-d). Fluorescent labeling further showed stronger incorporation of *HOXA11* RNA
128 into ENL-T1 droplets compared to T1-3A droplets (Fig. 2b, d), supporting that RNA-mediated droplet
129 enhancement is facilitated through interactions with the basic patch.
130

131 **RNA binding promotes ENL mutant condensate formation at endogenous target loci**

132 We previously showed that oncogenic ENL mutations induce condensate formation at highly specific
133 genomic targets in cells, driving aberrant gene activation and tumorigenesis[25,26]. These mutations thus
134 provide a tractable system to interrogate how specific features, such as RNA binding, affect condensate
135 formation and function in cells. We expressed doxycycline-inducible FLAG-tagged ENL variants at near-
136 endogenous levels in two human kidney-derived cell lines, HEK293 and WiT49 (Fig. 2e, f and Extended
137 Data Fig. 4a, b). We focused on two of the most common patient-derived mutants: ENL-T1 (insertion)
138 and ENL-T2 (deletion) (Fig. 1a), and generated RNA-binding-deficient T1-3A and T2-3A by introducing
139 the K61A/R63A/K67A triple mutation.

140 Consistent with previous findings, FLAG-ENL immunofluorescence (IF) revealed that ENL-T1 and
141 T2 formed discrete nuclear condensates not seen with ENL-WT (Fig. 2f-h and Extended Data Fig. 4b).
142 Notably, the 3A mutation significantly reduced the number of condensates per cell, indicating that RNA
143 binding promotes the ability of ENL-T1 and T2 to form condensates (Fig. 2f-h and Extended Data Fig.
144 4b). Cycloheximide chase assays showed comparable protein stability across all variants (Extended
145 Data Fig. 4c, d), indicating that the reduction in condensate formation is not simply due to differences in
146 protein turnover. These phenotypes were observed across additional cell lines, including A549 (lung
147 cancer) and MDA-MB-231 (breast cancer), where ENL-T1 and T2 again formed discrete nuclear
148 condensates while the 3A mutation reduced condensate number (Fig. 2i, j and Extended Data Fig. 4e-h).

149 To determine whether ENL:RNA interactions contribute to condensate formation at endogenous
150 target genes, we performed concurrent FLAG-ENL IF and DNA-FISH using probes targeting the *HOXA*
151 locus or *CBX3,* two key ENL-T1 and T2 target loci in kidney cell lines. In HEK293 cells expressing ENL-
152 T1 or T2, the majority of *HOXA* and *CBX3* DNA alleles colocalized with ENL mutant puncta (Fig. 2k-r),
153 indicating robust and frequent condensate formation at these loci. In contrast, colocalization was
154 markedly reduced in cells expressing T1-3A or T2-3A variants (Fig. 2k-r), consistent with a lower overall
155 number of nuclear condensates that likely reduces the frequency of condensate association at any given
156 target locus.
157 Corroborating our imaging data, chromatin immunoprecipitation followed by quantitative PCR
158 (ChIP–qPCR) showed that ENL-T1 and T2 exhibited markedly increased occupancy at *HOXA* and *CBX3*
159 relative to ENL-WT, and this enrichment was significantly reduced in T1-3A and T2-3A (Fig. 2s, t).
160 Importantly, isothermal titration calorimetry using purified YEATS domain proteins demonstrated that the
161 3A mutation does not impair histone acetylation binding affinity of the ENL-T1 or T2 YEATS domains
162 (Extended Data Fig. 4i), ruling out loss of histone acetylation recognition as the main cause of reduced
163 chromatin occupancy.
164 Together, these findings support a model in which ENL:RNA interactions, mediated in part
165 through the K61/R63/K67 basic patch within the YEATS domain, facilitate condensate formation and
166 chromatin engagement by oncogenic ENL mutants at endogenous target loci.
167
168 **RNA binding promotes re-nucleation of ENL condensates at target loci following acute chemical**
169 **displacement**
170 As disruption of ENL:RNA interactions via the 3A mutation reduces condensate number (Fig. 2g-j), we
171 hypothesized that RNA binding facilitates condensate nucleation. To directly test this, we established a
172 chemical-induced condensate displacement and wash-off system to visualize and quantify condensate
173 re-nucleation dynamics at endogenous targets (Fig. 3a). DNA-FISH combined with FLAG-ENL IF
174 showed that ENL-T1 condensates frequently colocalize with the *HOXA* locus in HEK293 cells at basal
175 conditions (Figs. 2k, l and 3a, left panel). To monitor condensate nucleation at this site, we first displaced

176 condensates using TDI-11055, a small-molecule inhibitor that competitively blocks the interaction
177 between the ENL YEATS domain and acetylated histones[26,35] (Fig. 3a, middle panel). Following inhibitor
178 wash-off, we tracked the re-formation of condensates at the *HOXA* locus over time in cells expressing
179 either ENL-T1 or the RNA-binding-deficient T1-3A mutant (Fig. 3a, right panel, b).
180 In ENL-T1–expressing cells, TDI-11055 treatment markedly reduced the percentage of *HOXA*
181 alleles associated with condensates compared to untreated controls. Upon wash-off, condensate
182 occupancy at *HOXA* loci recovered over a 10-hour period, reaching levels comparable to untreated
183 controls (Fig. 3c, d and Extended Data Fig. 5a). This was accompanied by restored expression of
184 *HOXA11* and *HOXA13* (Fig. 3e and Extended Data Fig. 5b). In contrast, recovery was impaired in T1-
185 3A–expressing cells, both in condensate nucleation and gene activation (Fig. 3c-e and Extended Data
186 Fig. 5a, b).
187 To further probe of the role of nascent transcripts in condensate nucleation, we applied
188 transcription inhibitors in the wash-off system (Fig. 3f, g). ENL-T1–expressing cells were pre-treated with
189 either DMSO or a transcription inhibitor 1 hour prior to TDI-11055 wash-off. In DMSO-treated cells,
190 condensates rapidly re-formed at the *HOXA* locus, with 50% of *HOXA* alleles showing condensate
191 association within 6 hours post wash-off (Fig. 3h, j). This re-formation was accompanied by largely
192 restored *HOXA11* and *HOXA13* expression (Fig. 3i, k and Extended Data Fig. 5c, d). In contrast, acute
193 transcription inhibition using Actinomycin D (blocks initiation) or DRB (blocks elongation) significantly
194 impaired condensate re-formation (Fig. 3h-k and Extended Data Fig. 5c, d).
195 Together, using a unique chemical strategy to acutely displace and monitor re-formation of
196 condensates at defined genomic loci, we show that both RNA-binding capability and ongoing
197 transcription are required for efficient nucleation of ENL-T1 condensates.
198
199 **RNA binding preferentially enhances ENL mutant occupancy at condensate-permissive loci**
200 Our DNA-FISH and ChIP-qPCR analyses showed that disrupting ENL:RNA interactions via the
201 3A mutation reduces chromatin occupancy of oncogenic ENL mutants at condensate-associated
202 genomic loci (Fig. 2k-r). To assess whether RNA binding contributes to ENL mutant occupancy genome-

203 wide or preferentially at specific targets, we performed ChIP-seq for FLAG-ENL variants in HEK293 cells.
204 ENL-T1 and T2 largely occupied the same genomic regions as ENL-WT but with increased occupancy
205 (Extended Data Fig. 6a, b), consistent with increased self-association conferred by these oncogenic
206 mutations[25]. Ranking ENL-T1 or ENL-T2 peaks by their ChIP-seq signal revealed a highly asymmetric
207 distribution, with fewer than 1% of peaks showing disproportionately high occupancy (Fig. 4a and
208 Extended Data Fig. 6c). These top-ranked peaks included validated condensate-associated targets such
209 as the *HOXA* cluster and *CBX3* (Fig. 2k-r). Using the inflection point of the ranked plot, we classified
210 ENL-T1 and ENL-T2 peaks into top- and low-bound groups (Fig. 4a, Extended Data Fig. 6c, and
211 Supplementary Table 4). Top-bound peaks showed a greater fold increase in ENL-T1 or T2 occupancy
212 relative to ENL-WT (Fig. 4b and Extended Data Fig. 6d), suggesting that these target sites are most
213 likely to associate with condensates (Fig. 4c).

214 We next asked whether RNA interactions contribute differentially to ENL chromatin occupancy at
215 top- versus low-bound sites. At low-bound sites, both T1 and T1-3A showed similarly increased
216 occupancy relative to WT, with minimal differences between the two (Fig. 4d-f). In contrast, T1-3A
217 exhibited significantly reduced occupancy relative to T1 at top-bound sites, indicating that RNA binding
218 selectively reinforces ENL-T1 occupancy at condensate-associated loci. Similar results were observed
219 for T2 versus T2-3A comparisons (Extended Data Fig. 6e-g).

220 To test whether this selective requirement is conserved across cellular contexts with distinct
221 condensate-associated targets, we performed ChIP–seq in MDA-MB-231 breast cancer cells expressing
222 FLAG-ENL variants. As in HEK293, ENL-T1 and ENL-T2 exhibited an asymmetric distribution of ChIP–
223 seq signals. However, the top-bound peaks differed substantially between the two cell lines, reflecting
224 cell type-specific targeting (Fig. 4g, Extended Data Fig. 7a, b, and Supplementary Tables 5, 6).
225 Nevertheless, top-bound peaks in MDA-MB-231 also showed a greater increase in occupancy in T1 and
226 T2 relative to WT (Fig. 4h and Extended Data Fig. 7c). To test whether these top-bound sites are indeed
227 associated with condensates, we performed DNA-FISH for two top targets, *NR2F2* and *CHD2,* and found
228 that ENL-T1 and T2 condensates frequently colocalized with these targets (Fig. 4i-k and Extended Data
229 Fig. 7d-h). As in HEK293, the 3A mutation reduced ENL-T1 and T2 occupancy more strongly at top-

230 bound than at low-bound sites (Fig. 4l-n and Extended Data Fig. 7i-k), further supporting the conclusion
231 that RNA binding preferentially promotes ENL chromatin engagement at condensate-permissive loci.
232 Together, these findings support a model in which oncogenic mutations amplify ENL occupancy at
233 pre-existing target sites, but only a small, cell type–specific subset are permissive to condensate
234 formation. Although the molecular features of these sites remain to be defined, RNA interactions appear
235 to contribute more to ENL occupancy at these sites, likely by facilitating condensate nucleation than
236 general chromatin binding.
237
238 **RNA binding enhances transcriptional bursting and gene activation at condensate-permissive**
239 **loci**
240 Given that ENL mutant condensates drive hyperactivation of target genes[25,26], we next asked
241 whether RNA binding contributes to this function. We performed RNA-seq in HEK293 and MDA-MB-231
242 cells expressing ENL-T1, T2, or their RNA-binding-deficient 3A variants. Gene set enrichment analysis
243 (GSEA) using ChIP–seq–defined top-bound genes (Fig. 4a, g, Extended Data Fig. 6c, 7b, and
244 Supplementary Tables 7, 8) revealed upregulation of these targets in ENL-T1 and T2 expressing cells
245 compared to WT (Fig. 4o, p and Extended Data Fig. 8a, b). This enrichment was attenuated in T1-3A and
246 T2-3A mutants (Fig. 4o, p and Extended Data Fig. 8a, b), indicating that RNA binding contributes to the
247 hyperactivation of condensate-associated targets. RT–qPCR for nascent transcripts confirmed reduced
248 expression of key targets in T1-3A and T2-3A–expressing cells relative to T1 and T2 in both cell lines
249 (Fig. 4q and Extended Data Fig. 8c, d).
250 To examine transcriptional activity at single-cell and single-allele resolution, we performed RNA-
251 FISH targeting intronic *HOXA13* transcripts with Halo-tagged ENL staining in HEK293 cells. ENL-T1 and
252 T2 expression led to a significant increase in detected RNA-FISH foci per cell compared to WT (Fig. 4r, s
253 and Extended Data Fig. 8e, f), indicative of increased transcription bursting frequency at the *HOXA*
254 locus. Notably, nearly all FISH foci in T1 or T2–expressing cells colocalized with condensates,
255 highlighting a strong link between condensate formation and transcriptional bursting (Fig. 4r-t and
256 Extended Data Fig. 8e-g). The T1 and T2-induced increase in RNA-FISH foci was largely abrogated by

257 the 3A mutation (Fig. 4r-t and Extended Data Fig. 8e-g). Although T1-3A and T2-3A cells showed fewer
258 RNA-FISH foci, those detected still colocalized with condensates and exhibited comparable intensities to
259 those observed in T1 or T2 cells (Fig. 4t and Extended Data Fig. 8g, h), reinforcing the link between
260 condensates and gene activation. Together, these results suggest that RNA binding primarily promotes
261 the frequency of condensate formation on target genes, thereby increasing transcriptional bursting
262 frequency and enabling robust gene activation by oncogenic ENL mutants.
263
264 **Disrupting RNA binding impairs ENL mutant–driven leukemogenesis**
265 We previously demonstrated that cancer-associated ENL mutations are bona fide drivers of AML using
266 both conditional knock-in mouse models and transplantation models of ectopic expression in
267 hematopoietic stem/progenitor cells (HSPCs)[26]. Building on this, we sought to determine whether RNA-
268 binding is required for the oncogenic activity of ENL mutants. We isolated LSK ($Lin^{-}Sca1^{+}cKit^{+}$) cells
269 from wildtype C57BL/6 mice and transduced them with FLAG-tagged ENL-WT, T1, or T1-3A constructs
270 (Fig. 5a), which were expressed at comparable RNA and protein levels (Extended Data Fig. 9a, b). FLAG
271 IF showed that ENL-T1 formed discrete condensates not seen with ENL-WT, while T1-3A exhibited a
272 marked reduction in condensate number (Fig. 5b, c). We next performed DNA-FISH targeting the *Hoxa*
273 cluster and *Meis1*, two key loci previously shown to colocalize with and are activated by ENL mutant
274 condensates in LSK cells[26]. Colocalization of these loci with ENL condensates was significantly more
275 frequent in T1 than in T1-3A–expressing cells (Fig. 5d-g), supporting that RNA binding promotes
276 condensate formation at critical leukemogenic gene loci in HSPCs.
277 To assess the transcriptional consequences of disrupting ENL:RNA interactions, we performed
278 RNA-seq in LSK cells expressing ENL-WT, T1, or T1-3A. Differential gene expression analysis (fold
279 change > 1.5; *padj* < 0.05) identified five gene clusters (Extended Data Fig. 9c and Supplementary Table
280 9). Consistent with ENL-T1 functioning as a transcriptional activator, most differentially expressed genes
281 (DEGs) were upregulated from WT to T1 (C3 and C5), while a smaller subset of DEGs were
282 downregulated (C1 and C2) (Extended Data Fig. 9c). Only a limited number of DEGs were uniquely
283 imparted by ENL-T1-3A (C4) (Extended Data Fig. 9c). Focusing on C3 and C5, which represent the

284 majority of DEGs and those upregulated by ENL-T1, we found that the 3A mutation impaired ENL-T1-
285 driven gene activation (Fig. 5h, i), including reduced expression of key condensate-associated targets,
286 the *Hoxa* cluster genes and *Meis1* (Fig. 5j).

287 Using our previously published ENL-T1 chromatin occupancy dataset generated in LSK cells[26],
288 we stratified ENL-T1-bound peaks into top- and low-bound groups (Extended Data Fig. 9d and
289 Supplementary Table 10). GSEA revealed that genes associated with top-bound peaks were significantly
290 upregulated in T1 versus WT and remained enriched in T1 compared to T1-3A (Fig. 5k and Extended
291 Fig. 9e). Moreover, genes associated with leukemic stem cells in AML patients were enriched in T1
292 relative to both WT and T1-3A (Fig. 5l and Extended Data Fig. 9f), indicating that RNA binding
293 contributes to ENL mutant-driven leukemogenic programs.

294 Finally, we assessed the impact of perturbing ENL:RNA interactions on leukemogenesis. We first
295 performed serial colony formation assays to evaluate self-renewal capacity. ENL-T1–expressing LSK
296 cells maintained robust colony-forming ability over multiple replatings, whereas WT and T1-3A cells
297 rapidly lost this potential (Fig. 5m), indicating that RNA binding is critical for sustaining the T1-induced
298 oncogenic state. We next transplanted LSK cells expressing ENL-WT, T1, or T1-3A into lethally irradiated
299 mice and monitored engraftment over time (Fig. 5n). All groups had similar initial engraftment at two
300 weeks post transplantation (Fig. 5o). However, at the terminal timepoint, defined by maximal disease
301 burden in ENL-T1 mice or one year post-transplantation for WT and T1-3A, ENL-T1 mice exhibited
302 significantly higher engraftment (Fig. 5o and Extended Data Fig. 9g) and markedly reduced survival
303 across two independent cohorts (Fig. 5p and Extended Data Fig. 9h). Postmortem analysis confirmed
304 hallmark AML features in ENL-T1 mice, including splenomegaly and leukemic blast infiltration into lung,
305 liver, and kidneys. In contrast, WT and T1-3A mice showed no signs of leukemia even one year post
306 transplantation (Fig. 5q, r). Together, these results demonstrate that ENL:RNA interactions are critical for
307 supporting the full oncogenic potential of cancer-associated ENL mutants in disease-relevant models.
308

309 **DISCUSSION**

310 Our findings reveal that RNA interactions actively promote the nucleation and oncogenic function
311 of chromatin-associated condensates. While ENL mutations are the primary trigger of condensate
312 formation[25], genetic and chemical perturbations demonstrate that RNA binding enhances condensate
313 nucleation efficiency at selective genomic loci. These interactions reinforce local enrichment of mutant
314 ENL—and likely associated co-factors—which amplifies transcriptional bursting and oncogenic activation
315 essential for tumorigenesis. This effect is particularly pronounced at condensate-permissive sites,
316 suggesting that condensates impose locus-specific transcriptional control through distinct, RNA-sensitive
317 mechanisms (Fig. 5s).

318 The positive role of RNA identified here in the context of pathogenic condensates contrasts with
319 models from normal cells, where accumulating RNA is thought to exert negative feedback on
320 transcription. For instance, while low levels of enhancer RNAs facilitate Mediator condensate formation
321 at super-enhancers in mouse embryonic stem cells, increasing levels of nascent RNA during
322 transcriptional bursts have been shown to disrupt condensates by altering the local electrostatic
323 balance[15,36]. Such feedback mechanisms likely serve to ensure proper gene expression during
324 development and to maintain homeostasis[36]. In contrast, cancer cells often depend on persistent
325 oncogene activation to maintain malignant states[37]. As exemplified by ENL mutations, one way to
326 achieve this is by co-opting condensates that both promote transcription and bypass RNA-mediated
327 negative feedback.

328 We propose that basal levels of nascent transcripts provide multivalent interactions that lower the
329 energetic barrier for condensate nucleation, enabling mutant ENL to efficiently concentrate at key
330 genomic targets and drive aberrant transcription. Elevated levels of locally produced RNA—rather than
331 triggering condensate dissolution—may be buffered through direct interactions with ENL and other
332 factors within the condensates. This buffering effect could further stabilize condensate association and
333 sustain high-level transcriptional output critical for tumorigenesis.

334 Beyond mutant ENL, other oncogenic drivers, such as NUP98-HOXA9, EWS-FLI1, and mutant
335 nucleophosmin (NPM1), also form condensates enriched in regulatory factors[6,38-42]. These proteins often
336 contain intrinsically disordered regions with charge blocks that may enable interactions with RNA[38,43,44].

337 Thus, we speculate that this RNA-dependent condensate regulation may represent a broader strategy
338 through which cancer cells achieve persistent pathogenic gene activation. While our study highlights how
339 RNA interactions promote condensate formation and function, condensates can also influence RNA fate.
340 For example, condensates formed by the m6A reader YTHDC1 were shown to protect *MYC* transcripts
341 from degradation in leukemia[45]. In other settings, high levels of nascent transcripts can suppress further
342 transcription from the same locus through autoregulatory mechanisms[46], independent of condensates. It
343 is therefore possible that pathogenic condensates might buffer these transcripts and bypass such
344 feedback, thereby enabling sustained transcription, a hypothesis warranting further investigation.

345 Together, our findings establish RNA as an active cofactor that pathogenic condensates can
346 exploit not only to promote their formation, but also to sustain aberrant transcriptional programs. This
347 feed-forward mechanism may represent a broadly used strategy in cancer and other diseases
348 characterized by persistent transcriptional dysregulation and could offer new avenues for mechanistic
349 understanding and therapeutic exploration.

350

351 **DATA AVAILABILITY**

352 All CLAP-seq, ChIP-seq, and RNA-seq raw and processed data have been deposited in the Gene
353 Expression Omnibus database under accession numbers GSE300418, GSE300420, GSE300421. All
354 other raw data generated or analyzed during this study are included in this paper, the Extended Data
355 Figures, and the Supplementary Information.

356

357 **ACKNOWLEDGEMENTS**

358 We thank members of the Wan Laboratory and the Li Laboratory for scientific input throughout the study;
359 the CDB Microscopy Core at the University of Pennsylvania; the Flow Cytometry and Cell Sorting Core at
360 the Children's Hospital of Pennsylvania; the Pathology Core at the Children's Hospital of Pennsylvania;
361 the AFCRI Research Facilities Team at the University of Pennsylvania, and the University Laboratory
362 Animal Resources team at the University of Pennsylvania. The research was supported by funding from

the University of Pennsylvania (to L.W.), NIH Director's New Innovator Award (1DP2HG012443, to L.W.), Pew-Stewart Scholar Award (to L.W.), American Cancer Society Award (to L.W.), Leukemia & Lymphoma Society Scholar Award (to L.W.), the National Key Research and Development Program of China (2022YFA1304800, to Y.Li; 2021YFA1300103, 2020YFA0803303, to H.L.), the National Natural Science Foundation of China (T2488301, 32230019, to H.L.), the American Cancer Society Postdoctoral Fellowship Award (to Y.Liu), and an F31 Predoctoral Fellowship (to K.M.M).

AUTHOR CONTRIBUTIONS

K.A.B, Y.Li, H.L., and L.W. conceived and designed the study. K.A.B performed the cellular, molecular, genomics, and *in vivo* animal studies. X.Y. and Y.Li performed *in vitro* biochemical studies. C.G. performed bioinformatic analysis of genomics data. Q.L. provided bioinformatics analysis pipelines. M.C.L., S.T., Y.Liu, L.S., and K.M.M. provided technical assistance. S.C.N. and E.F.J. designed and synthesized FISH probes. K.A.B. and L.W. wrote the manuscript with input from H.L., Y.Li, X.Y., L.S., and C.G. H.L. and Y.Li jointly supervised the *in vitro* biochemical studies. L.W. supervised the overall study.

COMPETING INTERESTS

L.W. is a co-inventor on a patent filed (US No. 62/949,160) related to the inhibitor used in this manuscript. All other authors declare no competing interests.

MATERIALS AND CORRESPONDENCE

Correspondence and requests for materials should be addressed to lead contact L.W. (liling.wan@pennmedicine.upenn.edu).

REFERENCES

1 Banani, S. F., Lee, H. O., Hyman, A. A. & Rosen, M. K. Biomolecular condensates: organizers of cellular biochemistry. *Nat Rev Mol Cell Biol* **18**, 285-298, doi:10.1038/nrm.2017.7 (2017).

2 Cho WK, S. J., Hecht M, Lee C, Li C, Grube V, Cisse II. Mediator and RNA polymerase II clusters associate in transcription-dependent condensates. *Science* **361**, doi:10.1126/science.aar4199 (2018).

3 Mir, M. *et al.* Dynamic multifactor hubs interact transiently with sites of active transcription in Drosophila embryos. *Elife* **7**, doi:10.7554/eLife.40497 (2018).

4 Hnisz, D., Shrinivas, K., Young, R. A., Chakraborty, A. K. & Sharp, P. A. A Phase Separation Model for Transcriptional Control. *Cell* **169**, 13-23, doi:10.1016/j.cell.2017.02.007 (2017).

5 Bhat, P., Honson, D. & Guttman, M. Nuclear compartmentalization as a mechanism of quantitative control of gene expression. *Nat Rev Mol Cell Biol* **22**, 653-670, doi:10.1038/s41580-021-00387-1 (2021).

6 Chong, S. *et al.* Imaging dynamic and selective low-complexity domain interactions that control gene transcription. *Science* **361**, doi:10.1126/science.aar2555 (2018).

7 Sabari, B. R. *et al.* Coactivator condensation at super-enhancers links phase separation and gene control. *Science* **361**, doi:10.1126/science.aar3958 (2018).

8 Lu, H. *et al.* Phase-separation mechanism for C-terminal hyperphosphorylation of RNA polymerase II. *Nature* **558**, 318-323, doi:10.1038/s41586-018-0174-3 (2018).

9 Boija, A., Klein, I. A. & Young, R. A. Biomolecular Condensates and Cancer. *Cancer Cell* **39**, 174-192, doi:10.1016/j.ccell.2020.12.003 (2021).

10 Xu, C., Kim, A., Corbin, J. M. & Wang, G. G. Onco-condensates: formation, multi-component organization, and biological functions. *Trends Cancer* **9**, 738-751, doi:10.1016/j.trecan.2023.05.006 (2023).

11 Mathias, K. M., Liu, Y. & Wan, L. Dysregulation of transcriptional condensates in human disease: mechanisms, biological functions, and open questions. *Curr Opin Genet Dev* **86**, 102203, doi:10.1016/j.gde.2024.102203 (2024).

12 Han, T. W., Portz, B., Young, R. A., Boija, A. & Klein, I. A. RNA and condensates: Disease implications and therapeutic opportunities. *Cell Chem Biol* **31**, 1593-1609, doi:10.1016/j.chembiol.2024.08.009 (2024).

13 Wadsworth, G. M. *et al.* RNA-driven phase transitions in biomolecular condensates. *Mol Cell* **84**, 3692-3705, doi:10.1016/j.molcel.2024.09.005 (2024).

14 Roden, C. & Gladfelter, A. S. RNA contributions to the form and function of biomolecular condensates. *Nat Rev Mol Cell Biol* **22**, 183-195, doi:10.1038/s41580-020-0264-6 (2021).

15 Henninger, J. E. *et al.* RNA-Mediated Feedback Control of Transcriptional Condensates. *Cell* **184**, 207-225 e224, doi:10.1016/j.cell.2020.11.030 (2021).

16 Asimi, V. *et al.* Hijacking of transcriptional condensates by endogenous retroviruses. *Nat Genet* **54**, 1238-1247, doi:10.1038/s41588-022-01132-w (2022).

17 Perlman, E. J. *et al.* MLLT1 YEATS domain mutations in clinically distinctive Favourable Histology Wilms tumours. *Nat Commun* **6**, 10013, doi:10.1038/ncomms10013 (2015).

18 Hetzner, K., Garcia-Cuellar, M.P., Buttner, C., and Slany, R.K. The interaction of ENL with PAF1 mitigates polycomb silencing and facilitates murine leukemogenesis. *Blood* **131** (2018).

19 Gadd, S. *et al.* A Children's Oncology Group and TARGET initiative exploring the genetic landscape of Wilms tumor. *Nat Genet* **49**, 1487-1494, doi:10.1038/ng.3940 (2017).

20 Umeda, M. *et al.* A new genomic framework to categorize pediatric acute myeloid leukemia. *Nat Genet* **56**, 281-293, doi:10.1038/s41588-023-01640-3 (2024).

21 Bolouri, H. *et al.* The molecular landscape of pediatric acute myeloid leukemia reveals recurrent structural alterations and age-specific mutational interactions. *Nat Med* **24**, 103-112, doi:10.1038/nm.4439 (2018).

22 Wan, L. *et al.* ENL links histone acetylation to oncogenic gene expression in acute myeloid leukaemia. *Nature* **543**, 265-269, doi:10.1038/nature21687 (2017).

23 Erb, M. A. *et al.* Transcription control by the ENL YEATS domain in acute leukaemia. *Nature* **543**, 270-274, doi:10.1038/nature21688 (2017).

24 Wan, L. *et al.* Impaired cell fate through gain-of-function mutations in a chromatin reader. *Nature* **577**, 121-126, doi:10.1038/s41586-019-1842-7 (2020).
25 Song, L. *et al.* Hotspot mutations in the structured ENL YEATS domain link aberrant transcriptional condensates and cancer. *Mol Cell* **82**, 4080-4098 e4012, doi:10.1016/j.molcel.2022.09.034 (2022).
26 Liu, Y. *et al.* Condensate-Promoting ENL Mutation Drives Tumorigenesis In Vivo Through Dynamic Regulation of Histone Modifications and Gene Expression. *Cancer Discov* **14**, 1522-1546, doi:10.1158/2159-8290.CD-23-0876 (2024).
27 Oksuz, O. *et al.* Transcription factors interact with RNA to regulate genes. *Mol Cell*, doi:10.1016/j.molcel.2023.06.012 (2023).
28 Bose, D. A. *et al.* RNA Binding to CBP Stimulates Histone Acetylation and Transcription. *Cell* **168**, 135-149 e122, doi:10.1016/j.cell.2016.12.020 (2017).
29 Rahnamoun, H. *et al.* RNAs interact with BRD4 to promote enhanced chromatin engagement and transcription activation. *Nat Struct Mol Biol* **25**, 687-697, doi:10.1038/s41594-018-0102-0 (2018).
30 Holmes, Z. E. *et al.* The Sox2 transcription factor binds RNA. *Nat Commun* **11**, 1805, doi:10.1038/s41467-020-15571-8 (2020).
31 Sigova, A. A., Abraham, B.J., Ji, X., Molinie, B., Hannett, N.M., Guo, Y.E., Jangi, M., Giallourakis, C.C., Sharp, P.A., and Young, R.A. . Transcription factor trapping by RNA in gene regulatory elements. *Science* **350**, 978–981, doi:https://doi.org/10.1126/science.aad3346. (2015).
32 Jeon, Y. & Lee, J. T. YY1 tethers Xist RNA to the inactive X nucleation center. *Cell* **146**, 119-133, doi:10.1016/j.cell.2011.06.026 (2011).
33 Klein, B. J. *et al.* Structural insights into the pi-pi-pi stacking mechanism and DNA-binding activity of the YEATS domain. *Nat Commun* **9**, 4574, doi:10.1038/s41467-018-07072-6 (2018).
34 Guo, J. K. *et al.* Denaturing purifications demonstrate that PRC2 and other widely reported chromatin proteins do not appear to bind directly to RNA in vivo. *Mol Cell* **84**, 1271-1289 e1212, doi:10.1016/j.molcel.2024.01.026 (2024).
35 Liu, Y. *et al.* Small-Molecule Inhibition of the Acyl-Lysine Reader ENL as a Strategy against Acute Myeloid Leukemia. *Cancer Discov* **12**, 2684-2709, doi:10.1158/2159-8290.CD-21-1307 (2022).
36 Ogami, K. *et al.* RNA Dynamics Regulate Transcriptional Condensate Vivacity to Drive Gene Coordination. *bioRxiv*, doi:10.1101/2025.06.06.658161 (2025).
37 Bradner, J. E., Hnisz, D. & Young, R. A. Transcriptional Addiction in Cancer. *Cell* **168**, 629-643, doi:10.1016/j.cell.2016.12.013 (2017).
38 Chandra, B. *et al.* Phase Separation Mediates NUP98 Fusion Oncoprotein Leukemic Transformation. *Cancer Discov* **12**, 1152-1169, doi:10.1158/2159-8290.CD-21-0674 (2022).
39 Wang, X. Q. D. *et al.* Mutant NPM1 Hijacks Transcriptional Hubs to Maintain Pathogenic Gene Programs in Acute Myeloid Leukemia. *Cancer Discov* **13**, 724-745, doi:10.1158/2159-8290.CD-22-0424 (2023).
40 Ahn, J. H. *et al.* The phenylalanine-and-glycine repeats of NUP98 oncofusions form condensates that selectively partition transcriptional coactivators. *Mol Cell* **85**, 708-725 e709, doi:10.1016/j.molcel.2024.12.026 (2025).
41 Ahn, J. H. *et al.* Phase separation drives aberrant chromatin looping and cancer development. *Nature* **595**, 591-595, doi:10.1038/s41586-021-03662-5 (2021).
42 Terlecki-Zaniewicz, S. *et al.* Biomolecular condensation of NUP98 fusion proteins drives leukemogenic gene expression. *Nat Struct Mol Biol* **28**, 190-201, doi:10.1038/s41594-020-00550-w (2021).
43 Selig, E. E., Romero-Moreno, A. K., Akula, S., Xu, X. & Libich, D. S. The oncogenic fusion protein EWS-FLI1 promotes premature ageing of biomolecular condensates by catalyzing fibril formation. *bioRxiv*, doi:10.1101/2022.06.04.494830 (2022).
44 Ng KP, P. G., Savene RO, Denny CT, Uversky VN, Lee KA. Multiple aromatic side chains within a disordered structure are critical for transcription and transforming activity of EWS family oncoproteins. *Proc Natl Acad Sci U S A* **104**, 479-484, doi:10.1073/pnas.0607007104. (2007).
45 Cheng, Y. *et al.* N(6)-Methyladenosine on mRNA facilitates a phase-separated nuclear body that suppresses myeloid leukemic differentiation. *Cancer Cell* **39**, 958-972 e958, doi:10.1016/j.ccell.2021.04.017 (2021).

46 Kaikkonen, M. U. & Adelman, K. Emerging Roles of Non-Coding RNA Transcription. *Trends Biochem Sci* **43**, 654-667, doi:10.1016/j.tibs.2018.06.002 (2018).

FIGURES AND FIGURE LEGENDS

Fig. 1

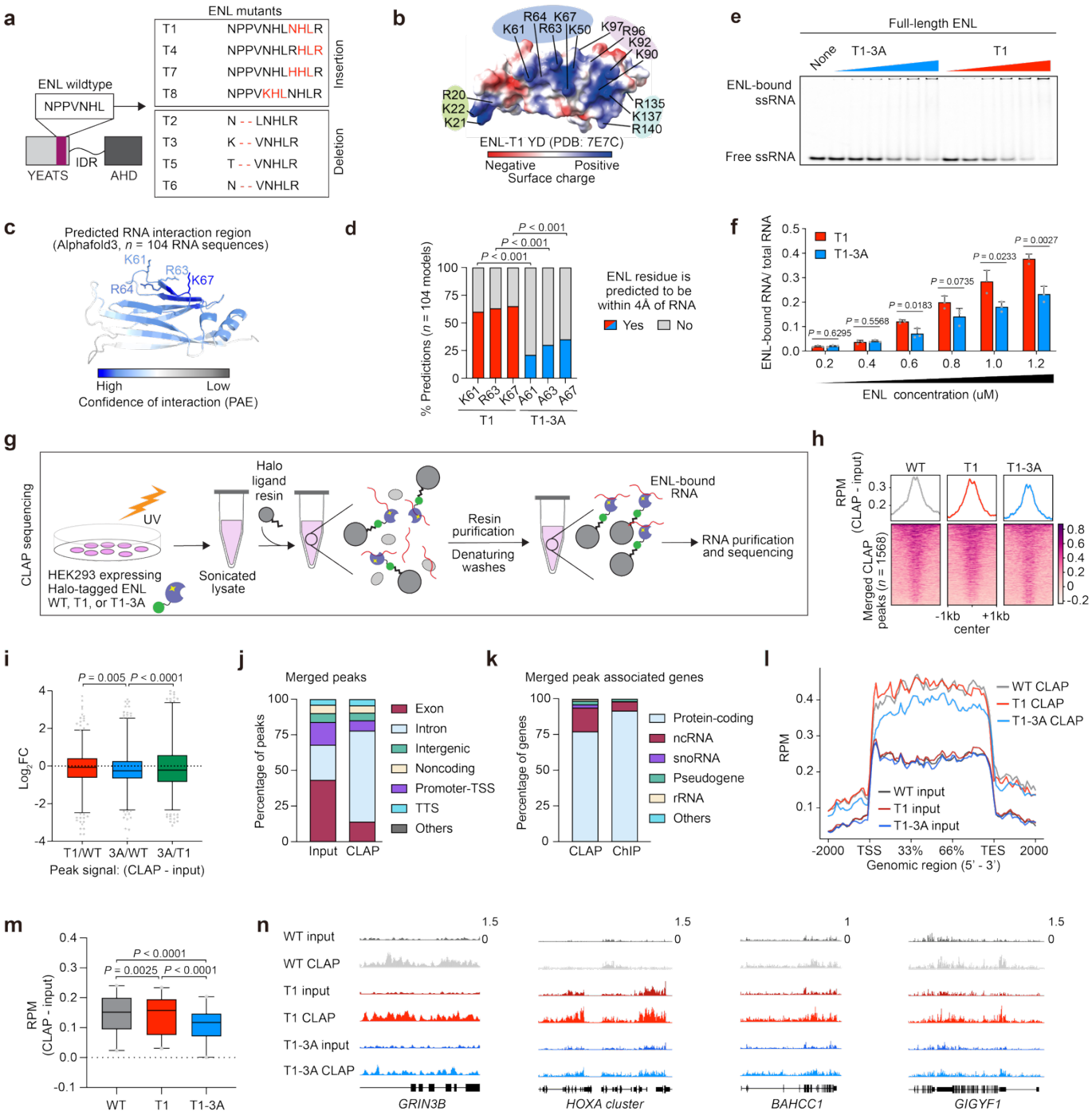

385 **Fig. 1. ENL binds RNA via a conserved basic patch in the YEATS domain. a,** Schematic of ENL
386 wildtype protein sequence and its oncogenic hotspot mutations, T1-T8. Mutations are shown in red text.
387 YEATS, Yaf9, Enl, Af9, Taf14, Sas5; IDR, intrinsically disordered region; AHD, ANC1 homology domain.
388 **b,** Surface charge map of ENL-T1 YEATS domain (YD). Residues from positive patches are labeled. **c,**
389 Heatmap depicting confidence scores (PAE, predicted aligned error) of predicted RNA-interacting
390 regions in the ENL-T1 YEATS domain. Predictions generated by Alphafold3. **d,** Percentage of Alphafold3
391 models in which indicated ENL residue is predicted to be within 4Å of the RNA molecule. *P* values were
392 calculated using two-tailed Fisher's exact test. **e,** Representative image of EMSA performed with purified
393 full-length ENL protein and a chemically synthesized 15nt *HOXA11* nascent RNA fragment. **f,** EMSA
394 quantification of ENL:RNA binding. Data are mean ± s.d. *P* values were calculated using two-tailed
395 unpaired Student's t test. Representative data shown for n = 3 replicates. **g,** Schematic of CLAP-
396 sequencing workflow. **h,** Average (top) and heatmap (bottom) representations of ENL-bound RNA signal
397 on merged WT, T1, and T1-3A CLAP peaks. Peak signals are calculated by subtracting input reads per
398 million (RPM) from those of corresponding CLAP pull-downs. **i,** Box plots showing Log_2 fold changes of
399 RNA peak signal on merged CLAP peaks. Center line indicates median, and box limits are set to 25th and
400 75th percentiles. *P* values were calculated using two-tailed paired Student's t test. **j,** Distribution of
401 merged input or CLAP pull-down RNA peaks across genomic regions. TSS, transcription start site; TTS,
402 transcription termination site. **k,** Distribution of peak-associated genes from merged ENL CLAP pull-
403 downs or ENL ChIP-seq. ncRNA, noncoding RNA; snoRNA, small nucleolar RNA; rRNA, ribosomal RNA.
404 **l,** RNA signal across gene body regions. RPM, reads per million; TSS, transcription start site; TES,
405 transcription end site. **m,** Box plots showing RNA signal (CLAP pull-downs relative to inputs) of peak-
406 associated genes. Center line indicates median, and box limits are set to 25th and 75th percentiles. *P*
407 values were calculated using two-tailed paired Student's t test. **n,** Genome browser view of ENL-bound
408 RNA signal in inputs and CLAP pull-downs.

Fig. 2

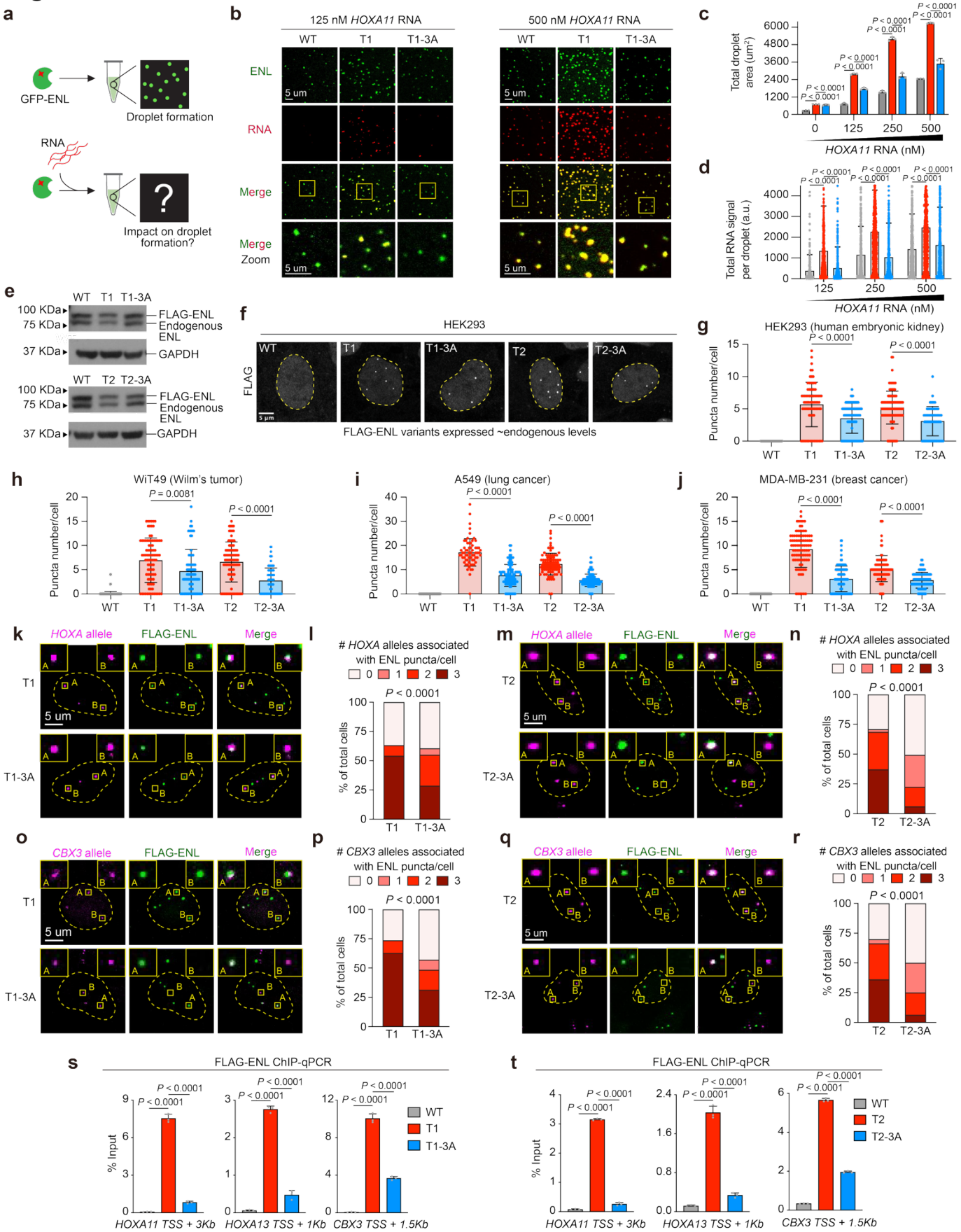
a
GFP-ENL
Droplet formation
RNA
?
Impact on droplet formation?
b
125 nM HOXA11 RNA
500 nM HOXA11 RNA
WT
T1
T1-3A
ENL
RNA
Merge
Merge Zoom
5 um
c
Total droplet area (um²)
HOXA11 RNA (nM)
d
Total RNA signal per droplet (a.u.)
HOXA11 RNA (nM)
e
WT T1 T1-3A
100 KDa
75 KDa
37 KDa
FLAG-ENL
Endogenous ENL
GAPDH
WT T2 T2-3A
f
HEK293
FLAG
WT
T1
T1-3A
T2
T2-3A
FLAG-ENL variants expressed ~endogenous levels
g
HEK293 (human embryonic kidney)
Puncta number/cell
h
WiT49 (Wilm's tumor)
i
A549 (lung cancer)
j
MDA-MB-231 (breast cancer)
k
HOXA allele
FLAG-ENL
Merge
l
HOXA alleles associated with ENL puncta/cell
% of total cells
m
n
o
CBX3 allele
p
CBX3 alleles associated with ENL puncta/cell
q
r
s
FLAG-ENL ChIP-qPCR
% Input
HOXA11 TSS + 3Kb
HOXA13 TSS + 1Kb
CBX3 TSS + 1.5Kb
t

409 **Fig. 2. Interactions with RNA promote condensate formation by oncogenic ENL.**

410 **a,** Schematic of *in vitro* droplet formation assay. **b,** *In vitro* droplet formation by purified recombinant
411 GFP-tagged ENL protein with two representative concentrations of chemically synthesized and
412 fluorescently labeled nascent *HOXA11* RNA. Yellow box indicates zoom-in region. **c,** Quantification of
413 total droplet area per image field. Data are mean ± s.d. *P* values were calculated by two-tailed unpaired
414 Student's t test. Representative data shown for *n* = 3 replicates. **d,** Total RNA signal (pixel intensity) per
415 ENL droplet. a.u., arbitrary units. Data are mean ± s.d. *P* values were calculated by two-tailed unpaired
416 Student's t test. Representative data shown for *n* = 3 replicates. **e,** Western blot showing similar
417 expression of ENL transgenes to each other and to endogenous ENL in HEK293 cells. **f,** Representative
418 IF staining of FLAG-ENL in HEK293 cells. Yellow dashed line outlines the nucleus. **g-j,** Quantification of
419 puncta number per cell in HEK293 (**g**), WiT49 (**h**), A549 (**i**), and MDA-MB-231 (**j**) cells. Data are mean ±
420 s.d. *P* values are calculated by two-tailed unpaired Student's t test. Representative data shown for *n* = 3
421 replicates. **k, m,** Representative *HOXA* DNA-FISH and FLAG-ENL IF staining in HEK293 cells. Yellow
422 dashed line outlines the nucleus **l, n,** Quantification of percentage of cells with indicated number of ENL
423 puncta-associated *HOXA* alleles. *P* values were calculated by two-tailed Fisher's exact test.
424 Representative data shown for *n* = 3 replicates. **o, q,** Representative *CBX3* DNA-FISH and FLAG-ENL IF
425 staining in HEK293 cells. Yellow dashed line outlines the nucleus **p, r,** Quantification of percentage of
426 cells with indicated number of ENL puncta-associated *CBX3* alleles. *P* values were calculated by two-
427 tailed Fisher's exact test. Representative data shown for *n* = 3 replicates. **s, t,** ChIP-qPCR analysis of
428 FLAG-ENL in HEK293 cells. Data are mean ± s.d. *P* values were calculated by two-tailed unpaired
429 Student's t test. Triplicate qPCR values are shown.

Fig. 3

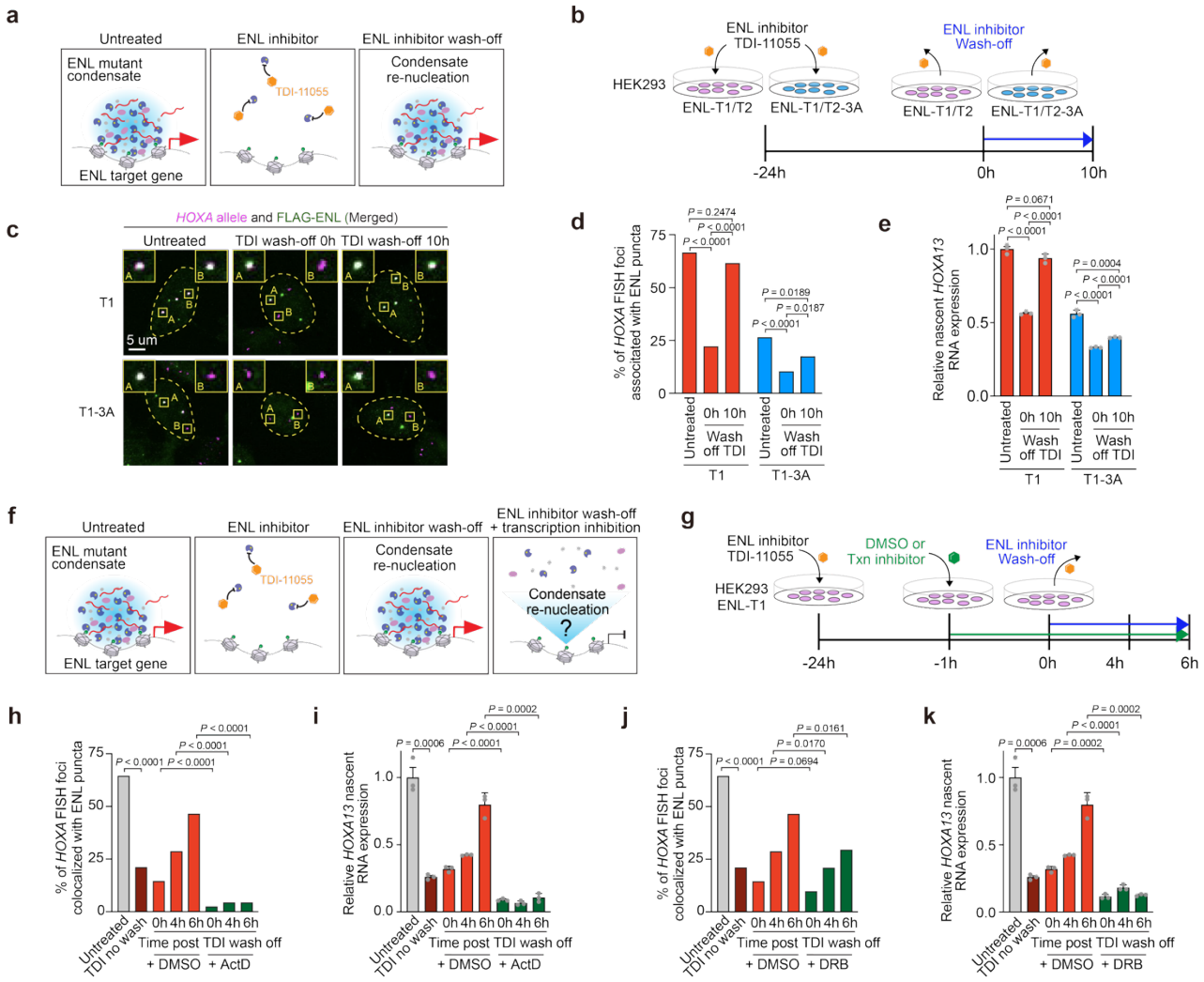
a
Untreated
ENL inhibitor
ENL inhibitor wash-off
ENL mutant condensate
TDI-11055
Condensate re-nucleation
ENL target gene
b
ENL inhibitor TDI-11055
ENL inhibitor Wash-off
HEK293
ENL-T1/T2
ENL-T1/T2-3A
-24h
0h
10h
c
HOXA allele and FLAG-ENL (Merged)
Untreated
TDI wash-off 0h
TDI wash-off 10h
T1
T1-3A
5 um
d
% of HOXA FISH foci associated with ENL puncta
P = 0.2474
P < 0.0001
P = 0.0189
P = 0.0187
Untreated
0h 10h
Wash off TDI
T1
T1-3A
e
Relative nascent HOXA13 RNA expression
P = 0.0671
P = 0.0004
f
ENL inhibitor wash-off + transcription inhibition
Condensate re-nucleation
?
g
DMSO or Txn inhibitor
HEK293 ENL-T1
-1h
4h
6h
h
% of HOXA FISH foci colocalized with ENL puncta
Untreated
TDI no wash
0h 4h 6h 0h 4h 6h
Time post TDI wash off
+ DMSO
+ ActD
i
Relative HOXA13 nascent RNA expression
P = 0.0006
P = 0.0002
j
P = 0.0161
P = 0.0170
P = 0.0694
+ DRB
k

Fig. 3. RNA binding facilitates dynamic re-nucleation of ENL condensates at key target loci after acute chemical displacement. a, Schematic depicting experimental design to measure condensate nucleation. Left panel shows ENL mutant condensates reliably occupying target genes. Middle panel shows ENL inhibitor TDI-11055 dislodging ENL condensates from target genes. Right panel shows TDI-11055 wash-off results in the reformation of ENL mutant condensates on target genes. **b,** Schematic of experimental workflow. **c,** Representative *HOXA* DNA-FISH and FLAG-ENL IF staining in HEK293 cells. Yellow dashed line outlines the nucleus. **d,** Quantification of percentage of total *HOXA* alleles associated with ENL mutant puncta in HEK293 cells. TDI, TDI-11055. *P* values were calculated by two-tailed Fisher's exact test. Representative data shown for $n = 3$ replicates. **e,** RT-qPCR showing nascent *HOXA13* expression relative to *GAPDH*. Data are mean ± s.d. *P* values were calculated by two-tailed unpaired Student's t test. Triplicate qPCR values are shown. **f,** Schematic depicting experimental design to measure condensate nucleation under transcription inhibition. **g,** Schematic of experimental workflow. **h, j,** Quantification of percentage of total *HOXA* alleles associated with ENL mutant puncta in HEK293 cells. TDI, TDI-11055; ActD, actinomycin D; DRB, 5,6-Dichloro-1-β-D-ribofuranosylbenzimidazole. *P* values were calculated by two-tailed Fisher's exact test. Representative data shown for $n = 3$ replicates. **i, k,** RT-qPCR showing nascent *HOXA13* expression relative to *18s rRNA*. Data are mean ± s.d. *P* values were calculated by two-tailed unpaired Student's t test. Representative data shown for $n = 3$ replicates.

Fig. 4

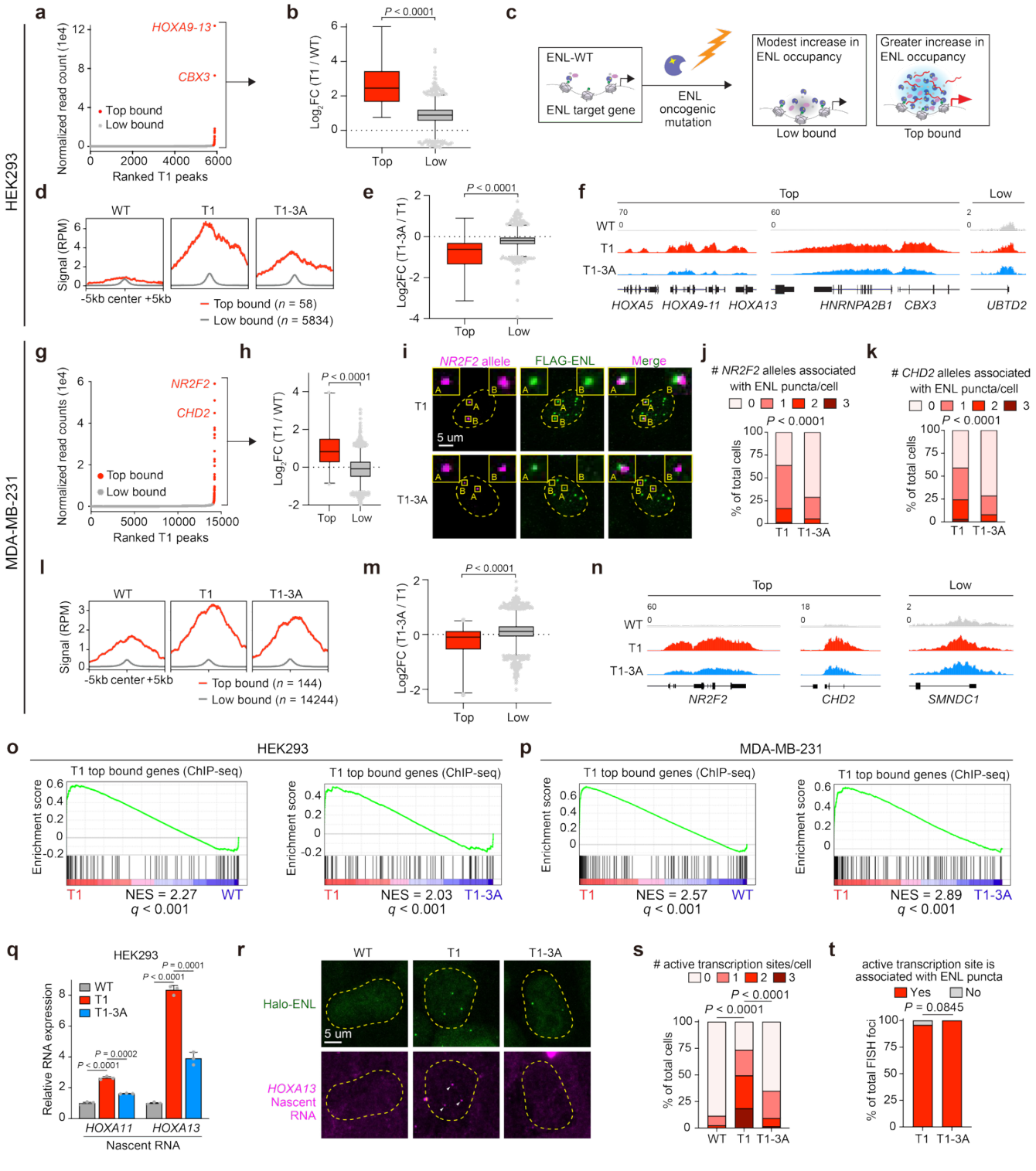
HEK293
MDA-MB-231
a
Normalized read count (1e4)
HOXA9-13
CBX3
Top bound
Low bound
Ranked T1 peaks
b
P < 0.0001
Log2FC (T1 / WT)
Top
Low
c
ENL-WT
ENL target gene
ENL oncogenic mutation
Modest increase in ENL occupancy
Low bound
Greater increase in ENL occupancy
Top bound
d
WT
T1
T1-3A
Signal (RPM)
-5kb center +5kb
Top bound (n = 58)
Low bound (n = 5834)
e
P < 0.0001
Log2FC (T1-3A / T1)
Top
Low
f
Top
Low
WT
T1
T1-3A
HOXA5
HOXA9-11
HOXA13
HNRNPA2B1
CBX3
UBTD2
g
Normalized read counts (1e4)
NR2F2
CHD2
Top bound
Low bound
Ranked T1 peaks
h
P < 0.0001
Log2FC (T1 / WT)
Top
Low
i
NR2F2 allele
FLAG-ENL
Merge
T1
T1-3A
5 um
j
NR2F2 alleles associated with ENL puncta/cell
0 1 2 3
P < 0.0001
% of total cells
T1
T1-3A
k
CHD2 alleles associated with ENL puncta/cell
0 1 2 3
P < 0.0001
% of total cells
T1
T1-3A
l
WT
T1
T1-3A
Signal (RPM)
-5kb center +5kb
Top bound (n = 144)
Low bound (n = 14244)
m
P < 0.0001
Log2FC (T1-3A / T1)
Top
Low
n
Top
Low
WT
T1
T1-3A
NR2F2
CHD2
SMNDC1
o
HEK293
T1 top bound genes (ChIP-seq)
Enrichment score
T1
NES = 2.27
q < 0.001
WT
T1 top bound genes (ChIP-seq)
Enrichment score
T1
NES = 2.03
q < 0.001
T1-3A
p
MDA-MB-231
T1 top bound genes (ChIP-seq)
Enrichment score
T1
NES = 2.57
q < 0.001
WT
T1 top bound genes (ChIP-seq)
Enrichment score
T1
NES = 2.89
q < 0.001
T1-3A
q
HEK293
WT
T1
T1-3A
P = 0.0001
P < 0.0001
P = 0.0002
P < 0.0001
Relative RNA expression
HOXA11
HOXA13
Nascent RNA
r
WT
T1
T1-3A
Halo-ENL
5 um
HOXA13 Nascent RNA
s
active transcription sites/cell
0 1 2 3
P < 0.0001
P < 0.0001
% of total cells
WT
T1
T1-3A
t
active transcription site is associated with ENL puncta
Yes
No
P = 0.0845
% of total FISH foci
T1
T1-3A

448 **Fig. 4. RNA binding preferentially promotes ENL mutant occupancy at condensate-permissive**
449 **target loci and enhances transcriptional bursting and gene expression. a,** ENL-T1 ChIP-seq peaks
450 in HEK293 cells ranked by read count. Top-bound peaks fall to the right of the inflection point and are
451 labeled in red text. Low-bound peaks fall to the left of the inflection point and are labeled in gray. Known
452 condensate-associated targets, *HOXA* and *CBX3*, are labeled in red text. **b,** Box plot showing Log_2 fold
453 change of T1/WT signal at top or low-bound sites in HEK293. Top, n = 58; Low, n = 5834. Center line
454 indicates median and box limits are set to 25th and 75th percentiles. P values were calculated by two-
455 tailed unpaired Student's t test. **c,** Schematic showing at that most ENL-bound sites (low-bound sites),
456 ENL-T1 modestly gains occupancy compared to ENL-WT. At a very small subset of ENL bound sites
457 (top-bound sites), ENL-T1 exhibits a large gain in chromatin occupancy, likely reflecting gain of
458 condensate formation. **d,** Average chromatin occupancy of ENL at top or low-bound sites. RPM, reads
459 per million. **e,** Box plot showing Log_2 fold change of T1-3A vs. T1 signal at top or low-bound sites. Top, n
460 = 58; Low, n = 5834. Center line indicates median and box limits are set to 25th and 75th percentiles. P
461 values were calculated by two-tailed unpaired Student's t test. **f,** Genome browser view of ENL ChIP
462 signal at representative HEK293 top and low-bound genes. **g,** ENL-T1 ChIP-seq peaks in MDA-MB-231
463 cells ranked by normalized read count. Top-bound peaks fall to the right of the inflection point and are
464 labeled in red text. Low-bound peaks fall to the left of the inflection point and are labeled in gray. **h,** Box
465 plot showing Log_2 fold change of T1/WT signal at top or low-bound sites in MDA-MB-231. Top, n = 144;
466 Low, n = 14244. Center line indicates median and box limits are set to 25th and 75th percentiles. P values
467 were calculated by two-tailed unpaired Student's t test. **i,** Representative *NR2F2* DNA-FISH and FLAG-
468 ENL IF staining in MDA-MB-231 cells. Yellow dashed line outlines the nucleus. **j, k,** Quantification of
469 percentage of cells with indicated number of ENL puncta-associated *NR2F2* (**j**) or *CHD2* (**k**) alleles. P
470 values were calculated by two-tailed Fisher's exact test. Representative data shown for n = 2 replicates.
471 **l,** Average chromatin occupancy of ENL at top or low-bound sites in MDA-MB-231 cells. RPM, reads per
472 million. **m,** Box plot showing Log_2 fold change of T1-3A/T1 signal at top or low-bound sites. Top, n = 144;
473 Low, n = 14244. Center line indicates median and box limits are set to 25th and 75th percentiles. P values
474 were calculated by two-tailed unpaired Student's t test. **n,** Genome browser view of ENL ChIP signal at

475 representative MDA-MB-231 top and low-bound genes. **o, p,** GSEA plots showing that top-bound genes
476 (determined by ChIP-seq) are upregulated in T1 compared to WT or to T1-3A in HEK293 (**o**) and MDA-
477 MB-231 (**p**) cells. NES, normalized enrichment score. **q,** RT-qPCR showing nascent *HOXA11* or
478 *HOXA13* expression relative to *GAPDH*. Data are mean ± s.d. *P* values were calculated by two-tailed
479 unpaired Student's t test. Triplicate qPCR values are shown. **r,** Representative nascent RNA-FISH for the
480 *HOXA13* locus and Halo staining for Halo-ENL in HEK293 cells. White arrows indicate RNA-FISH foci.
481 Yellow dashed line outlines the nucleus. **s,** Quantification of percentage of cells with indicated number of
482 nascent RNA-FISH foci. *P* values were calculated by two-tailed Fisher's exact test. Representative data
483 shown for n = 3 replicates. **t,** Quantification of percentage of total *HOXA13* FISH foci associated with
484 ENL mutant puncta. *P* values were calculated by two-tailed Fisher's exact test. Representative data
485 shown for n = 3 replicates.

Fig. 5

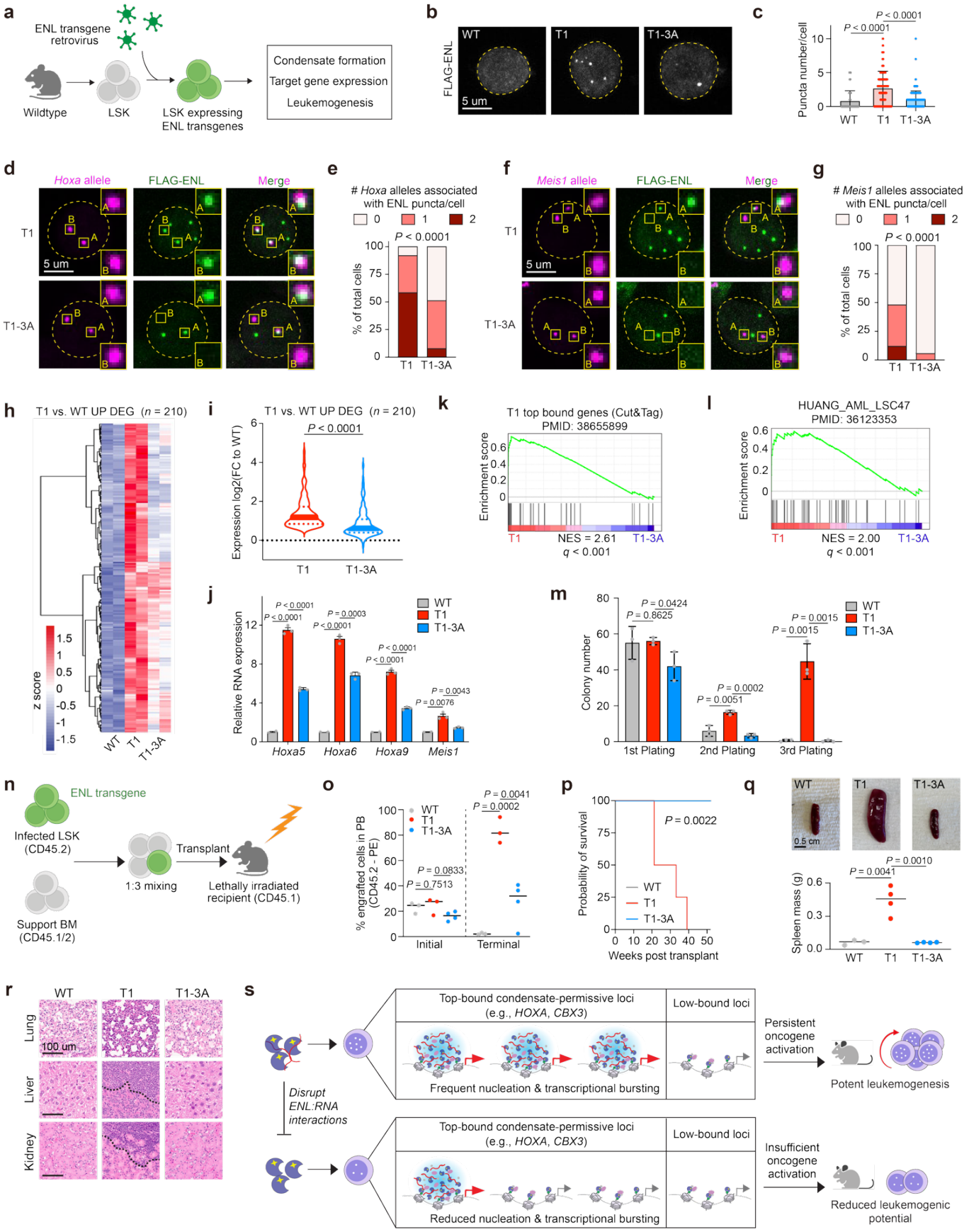
a
ENL transgene retrovirus
Wildtype
LSK
LSK expressing ENL transgenes
Condensate formation
Target gene expression
Leukemogenesis
b
FLAG-ENL
WT
T1
T1-3A
5 um
c
Puncta number/cell
P < 0.0001
WT
T1
T1-3A
d
Hoxa allele
FLAG-ENL
Merge
T1
T1-3A
5 um
e
Hoxa alleles associated with ENL puncta/cell
% of total cells
P < 0.0001
f
Meis1 allele
FLAG-ENL
Merge
g
Meis1 alleles associated with ENL puncta/cell
% of total cells
P < 0.0001
h
T1 vs. WT UP DEG (n = 210)
z score
WT
T1
T1-3A
i
T1 vs. WT UP DEG (n = 210)
Expression log2(FC to WT)
P < 0.0001
k
T1 top bound genes (Cut&Tag)
PMID: 38655899
Enrichment score
NES = 2.61
q < 0.001
l
HUANG_AML_LSC47
PMID: 36123353
Enrichment score
NES = 2.00
q < 0.001
j
Relative RNA expression
Hoxa5
Hoxa6
Hoxa9
Meis1
m
Colony number
1st Plating
2nd Plating
3rd Plating
n
ENL transgene
Infected LSK (CD45.2)
Support BM (CD45.1/2)
1:3 mixing
Transplant
Lethally irradiated recipient (CD45.1)
o
% engrafted cells in PB (CD45.2 - PE)
Initial
Terminal
p
Probability of survival
P = 0.0022
Weeks post transplant
q
0.5 cm
Spleen mass (g)
P = 0.0010
r
Lung
Liver
Kidney
100 um
s
Top-bound condensate-permissive loci (e.g., HOXA, CBX3)
Low-bound loci
Frequent nucleation & transcriptional bursting
Persistent oncogene activation
Potent leukemogenesis
Disrupt ENL:RNA interactions
Reduced nucleation & transcriptional bursting
Insufficient oncogene activation
Reduced leukemogenic potential

486 **Fig. 5. RNA binding is required for ENL mutant–driven leukemogenesis. a,** Experimental work flow
487 using hematopoietic stem cells (LSK). LSK, $Lin^{-}Sca^{+}cKit^{+}$. **b,** Representative FLAG-ENL IF staining in
488 LSK cells. Yellow dashed line outlines the nucleus**. c,** Quantification of puncta number per cell. Data are
489 mean ± s.d. *P* values were calculated by two-tailed unpaired Student's t test. **d, f,** Representative *Hoxa*
490 (**d**) or *Meis1* (**f**) DNA-FISH and FLAG-ENL IF staining in LSK cells. Yellow dashed line outlines the
491 nucleus. **e, g,** Quantification of percentage of cells with indicated number of ENL puncta-associated
492 *Hoxa* (**e**) or *Meis1* (**g**) alleles. *P* values were calculated by two-tailed Fisher's exact test. **h,** Heatmap
493 depicting z-scores of genes upregulated in T1 vs. WT LSK cells. DEG, differentially expressed genes. **i,**
494 Log2 fold change in expression of T1 vs. WT upregulated genes. Center line indicates median and red or
495 blue dotted lines indicate interquartile range. *P* values were calculated by two-tailed paired Student's t
496 test. **j,** RT-qPCR showing gene expression of key target loci relative to *Gapdh*. Data are mean ± s.d. *P*
497 values were calculated by two-tailed unpaired Student's t test. Triplicate qPCR values are shown **k,**
498 GSEA plot showing that ENL-T1 top-bound genes (Extended Data Fig. 9d, *n* = 69) are upregulated in T1
499 compared to T1-3A in LSK. NES, normalized enrichment score. **l,** GSEA plot showing that genes
500 associated with AML patients (*n* = 47) are upregulated in T1 compared to T1-3A in LSK. NES, normalized
501 enrichment score. **m,** Quantification of colonies formed by LSK expressing indicated ENL variants. Data
502 are mean ± s.d. *P* values were calculated by two-tailed unpaired Student's t test. Representative data
503 shown for *n* = 3 replicates. **n,** Schematic depicting experimental workflow for bone marrow (BM)
504 transplantation. CD45.1, CD45.2, CD45.1/2 represent leukocyte markers. **o,** Percentage of peripheral
505 blood (PB) composed of cells derived from transplanted LSK at initial versus terminal timepoints. Each
506 dot represents *n* = 1 mouse. Horizontal line represents median. *P* values were calculated using two-tailed
507 unpaired Student's t test. **p,** Kaplan-Meier survival curves of mice receiving bone marrow transplant. *P*
508 value was calculated using Mantel-Cox log-rank test. WT, *n* = *3*; T1, *n* = 4; T1-3A, *n* = *4.* **q,**
509 Representative images (top) and quantification (bottom) of spleen masses harvested from transplanted
510 mice. Each dot represents *n* = 1 spleen. Horizontal line represents median. *P* values were calculated
511 using two-tailed unpaired Student's t test. **r,** H&E staining. Black dashed line indicates leukemic blast
512 infiltration border. **s,** Model (top) ENL:RNA interactions facilitate condensate formation at key target

genes, thus driving frequent transcriptional bursting and persistent activation at top-bound, condensate-permissive loci, leading to potent leukemogenesis in mouse models. (Bottom) Disrupting these interactions reduces condensate nucleation, transcriptional bursting, and gene activation, ultimately impairing tumorigenesis.

Extended Data Fig. 1

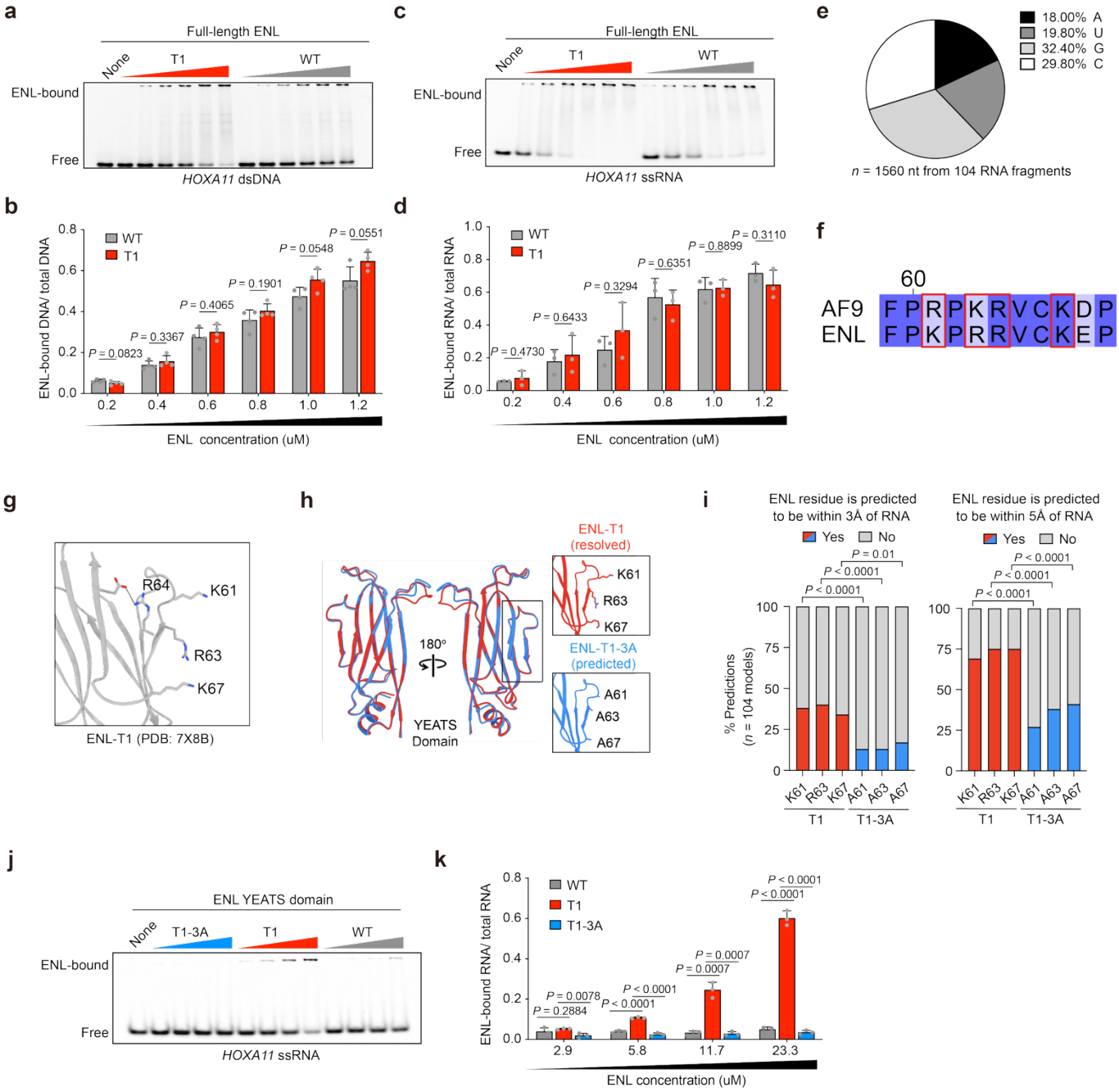

517 **Extended Data Fig. 1. ENL binds RNA via a conserved basic patch in the YEATS domain *in vitro*.**
518 **a, b,** Representative image (**a**) and quantification (**b**) of EMSA performed with purified full-length ENL
519 protein and chemically synthesized 15nt *HOXA11* dsDNA fragment. Data are mean ± s.d. *P* values were
520 calculated using two-tailed unpaired Student's t test. Representative data shown for *n* = 3 replicates. **c,**
521 **d,** Representative image (**c**) and quantification (**d**) of EMSA performed with purified full-length ENL
522 protein and chemically synthesized 15nt *HOXA11* ssRNA fragment. Data are mean ± s.d. *P* values were
523 calculated using two-tailed unpaired Student's t test. Representative data shown for *n* = 3 replicates. **e,**
524 Distribution of nucleotides in 104 RNA sequences used for Alphafold3 modelling. **f,** Sequence alignment
525 of ENL and ENL paralog, AF9. AF9's DNA-binding residues are outlined in red. **g,** ENL-T1 structure
526 shows K61, R63, and K67 are surface-exposed, while R64 is less accessible. **h,** Overlay of resolved
527 ENL-T1 and predicted ENL-T1-3A YEATS domain structures. T1-3A structure predicted with Alphafold3.
528 **i,** Percentage of Alphafold3 models in which indicated ENL residue is predicted to be within 3Å or 5Å of
529 the RNA molecule. *P* values were calculated using two-tailed Fisher's exact test. **j, k,** Representative
530 image (**j**) and quantification (**k**) of EMSA performed with purified ENL YEATS domain protein and *in vitro*
531 transcribed 15nt *HOXA11* ssRNA fragment. Data are mean ± s.d. *P* values were calculated using two-
532 tailed unpaired Student's t test. Representative data shown for *n* = 3 replicates.

Extended Data Fig. 2

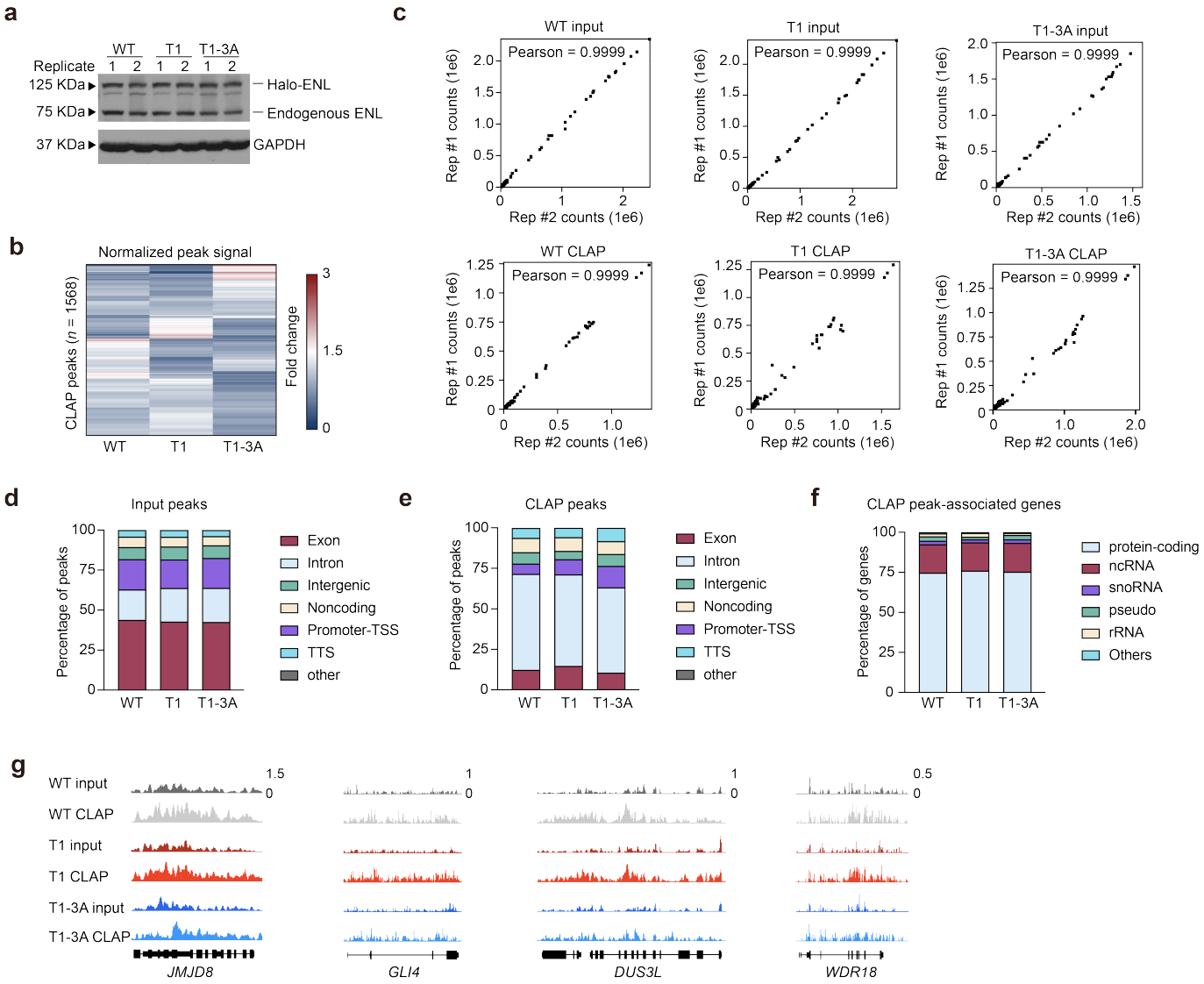

533 **Extended Data Fig. 2. ENL binds RNA via a conserved basic patch in the YEATS domain in cells.**
534 **a,** Western blot showing comparable expression of ENL transgenes to each other and to endogenous
535 ENL in HEK293 cells. **b,** Fold change values of peak signal within each sample over the average signal
536 across WT, T1, and T1-3A conditions. **c,** Pearson correlation analysis of CLAP experimental replicates.
537 Each dot represents the read counts per 5kb genomic bin per chromosome. **d,** Distribution of merged
538 input RNA peaks across genomic regions. TSS, transcription start site; TTS, transcription termination
539 site. **e,** Distribution of merged CLAP pull-down RNA peaks across genomic regions. TSS, transcription
540 start site; TTS, transcription termination site. **f,** Distribution of genes associated with ENL CLAP pull-
541 down peaks. ncRNA, noncoding RNA; snoRNA, small nucleolar RNA; rRNA, ribosomal RNA.

Extended Data Fig. 3

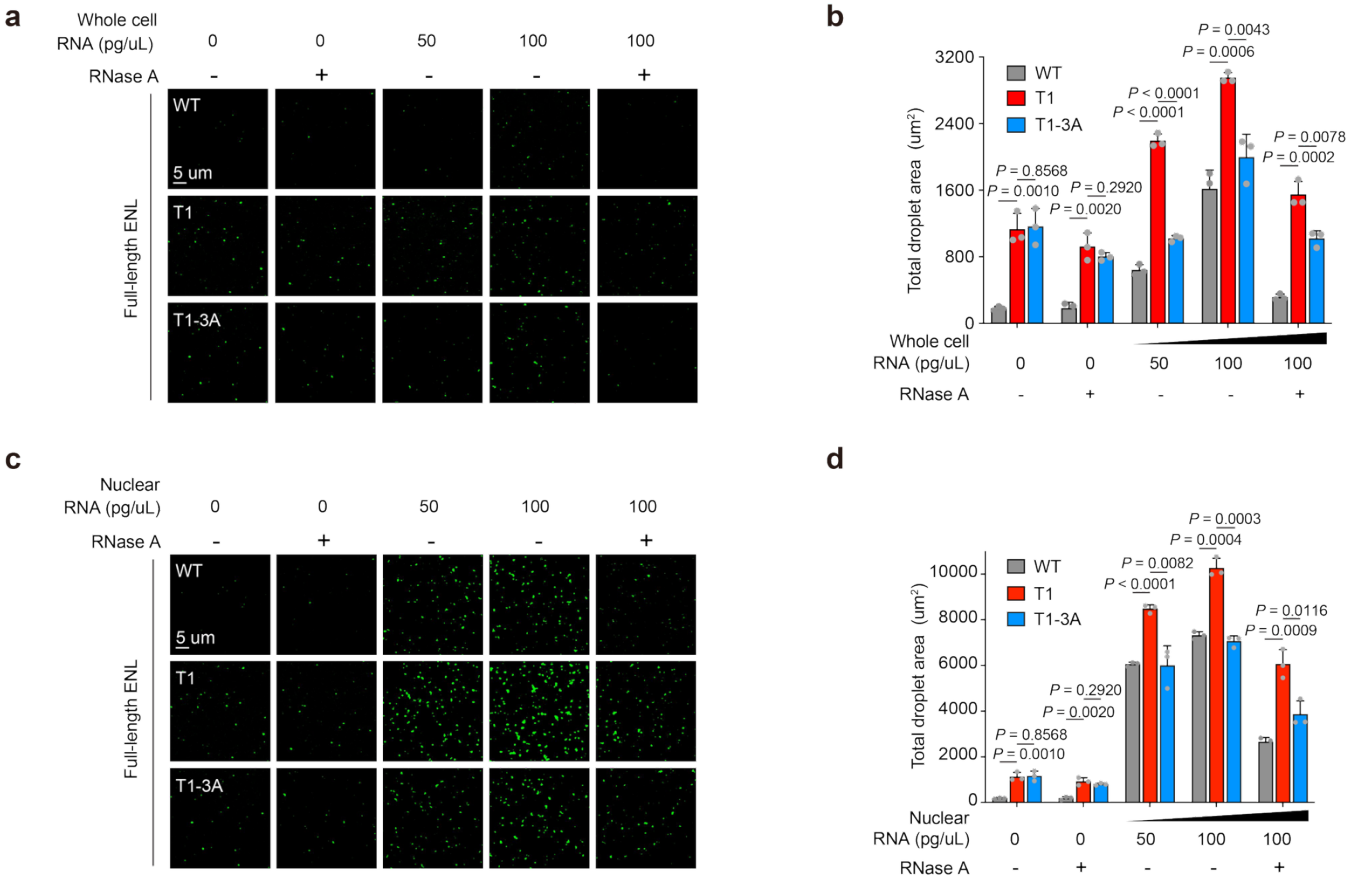

542 **Extended Data Fig. 3. RNA enhances droplet formation of purified ENL protein. a,** *In vitro* droplet
543 formation by purified recombinant GFP-tagged ENL protein with RNA extracted from whole cell lysate. **b,**
544 Quantification of total droplet area per image field. Data are mean ± s.d. *P* values were calculated by
545 two-tailed unpaired Student's t test. Representative data shown for *n* = 3 replicates. **c,** *In vitro* droplet
546 formation by purified recombinant GFP-tagged ENL protein with RNA extracted from cell nuclei. **d,**
547 Quantification of total droplet area per image field. Data are mean ± s.d. *P* values were calculated by
548 two-tailed unpaired Student's t test. Representative data shown for *n* = 3 replicates.

Extended Data Fig. 4

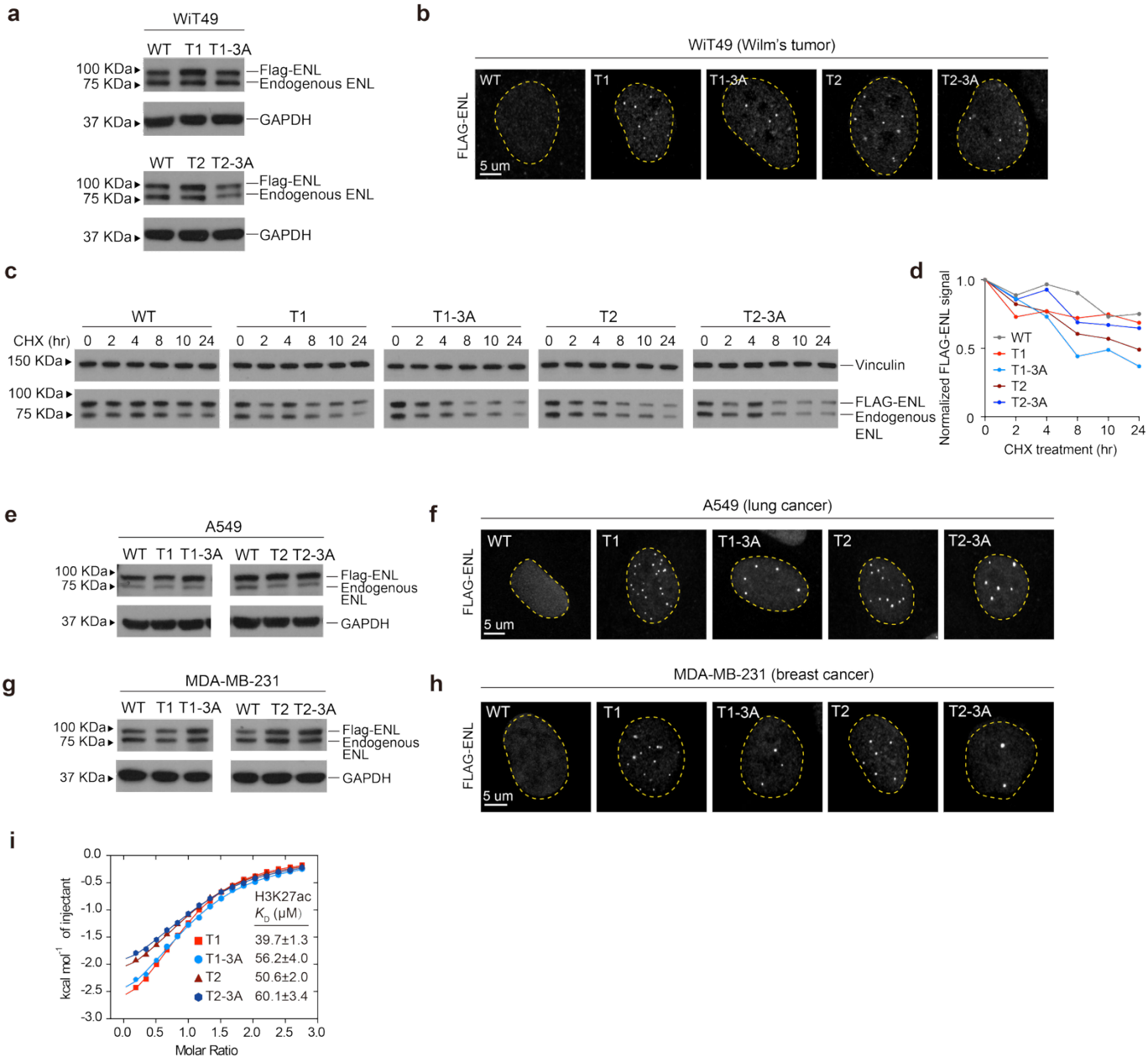

549 **Extended Data Fig. 4. RNA binding enhances condensate formation by oncogenic ENL at**
550 **endogenous target loci. a,** Western blot showing similar expression of ENL transgenes to each other
551 and to endogenous ENL in WiT49 cells. **b,** Representative IF staining of FLAG-ENL in WiT49 cells.
552 Yellow dashed line outlines the nucleus. **c,** Western blots of cycloheximide (CHX) pulse-chase assays. **d,**
553 Quantification of cycloheximide pulse chase assay. FLAG-ENL intensity at each time point is normalized
554 to matched vinculin intensity. **e, g,** Western blot showing similar expression of ENL transgenes to each
555 other and to endogenous ENL in A549 (**e**) and MDA-MB-231 (**g**) cells. **f, h,** Representative IF staining of
556 FLAG-ENL in A549 (**f**) and MDA-MB-231 (**h**) cells. Yellow dashed line outlines the nucleus. **i,** Isothermal
557 calorimetry of purified ENL protein and H3K27ac peptide.

Extended Data Fig. 5

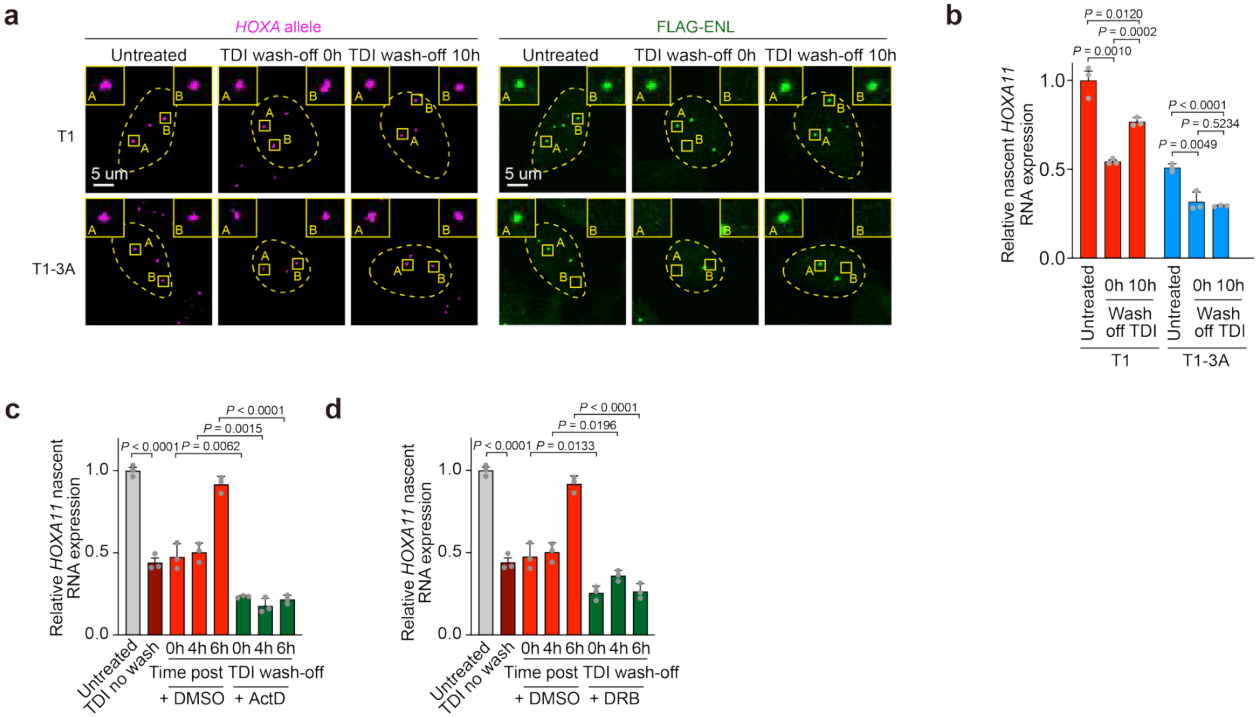

558 **Extended Data Fig. 5. RNA binding facilitates dynamic re-nucleation of ENL condensates at**
559 **endogenous target loci targets. a,** Representative *HOXA* DNA-FISH and FLAG-ENL IF staining in
560 HEK293 cells. Yellow dashed line outlines the nucleus. **b,** RT-qPCR showing nascent *HOXA11*
561 expression relative to *GAPDH*. Data are mean ± s.d. *P* values were calculated by two-tailed unpaired
562 Student's t test. **c, d,** RT-qPCR showing nascent *HOXA11* expression relative to *18S rRNA*. Data are
563 mean ± s.d. *P* values were calculated by two-tailed unpaired Student's t test.

Extended Data Fig. 6

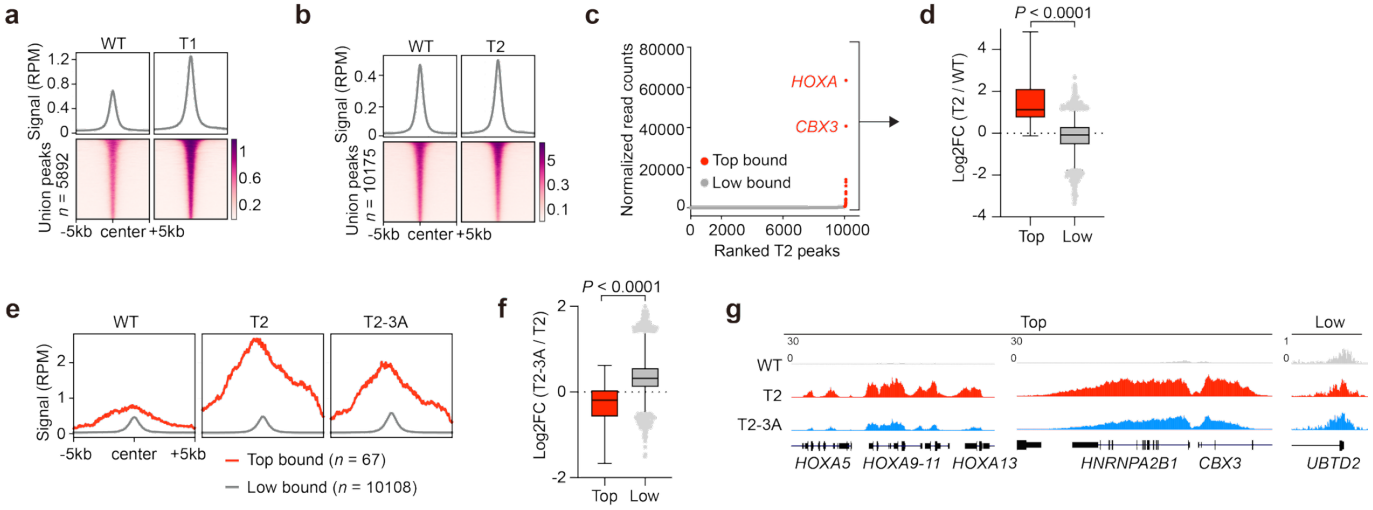

564 **Extended Data Fig. 6. RNA binding enhances mutant ENL occupancy at condensate-permissive**
565 **loci in HEK293 cells. a,** Average (top) and heatmap (bottom) representations of ENL ChIP signal on
566 merged ENL-WT/T1 peaks in HEK293 cells. RPM, reads per million. **b,** Average (top) and heatmap
567 (bottom) representations of ENL ChIP signal on merged ENL-WT/T2 peaks. RPM, reads per million. **c,**
568 ENL-T2 ChIP-seq peaks in HEK293 cells ranked by normalized read count. Top-bound peaks fall to the
569 right of the inflection point and are labeled in red text. Low-bound peaks fall to the left of the inflection
570 point and are labeled in gray. Known condensate-associated targets, *HOXA* and *CBX3*, are labeled in
571 red text. **d,** Box plot showing Log_2 fold change of T2/WT signal at top- or low-bound sites in HEK293.
572 Top, n = 67; Low, n = 10108. Center line indicates median and box limits are set to 25th and 75th
573 percentiles. P values were calculated by two-tailed unpaired Student's t test. **e,** Average chromatin
574 occupancy of ENL at top or low-bound sites in HEK293 cells. RPM, reads per million. **f,** Box plot showing
575 Log_2 fold change of T2-3A/T2 signal at top or low-bound sites in HEK293. Top, n = 67; Low, n = 10108.
576 Center line indicates median and box limits are set to 25th and 75th percentiles. P values were calculated
577 by two-tailed unpaired Student's t test. **g,** Genome browser view of ENL ChIP signal at representative
578 HEK293 top and low-bound genes.

Extended Data Fig. 7

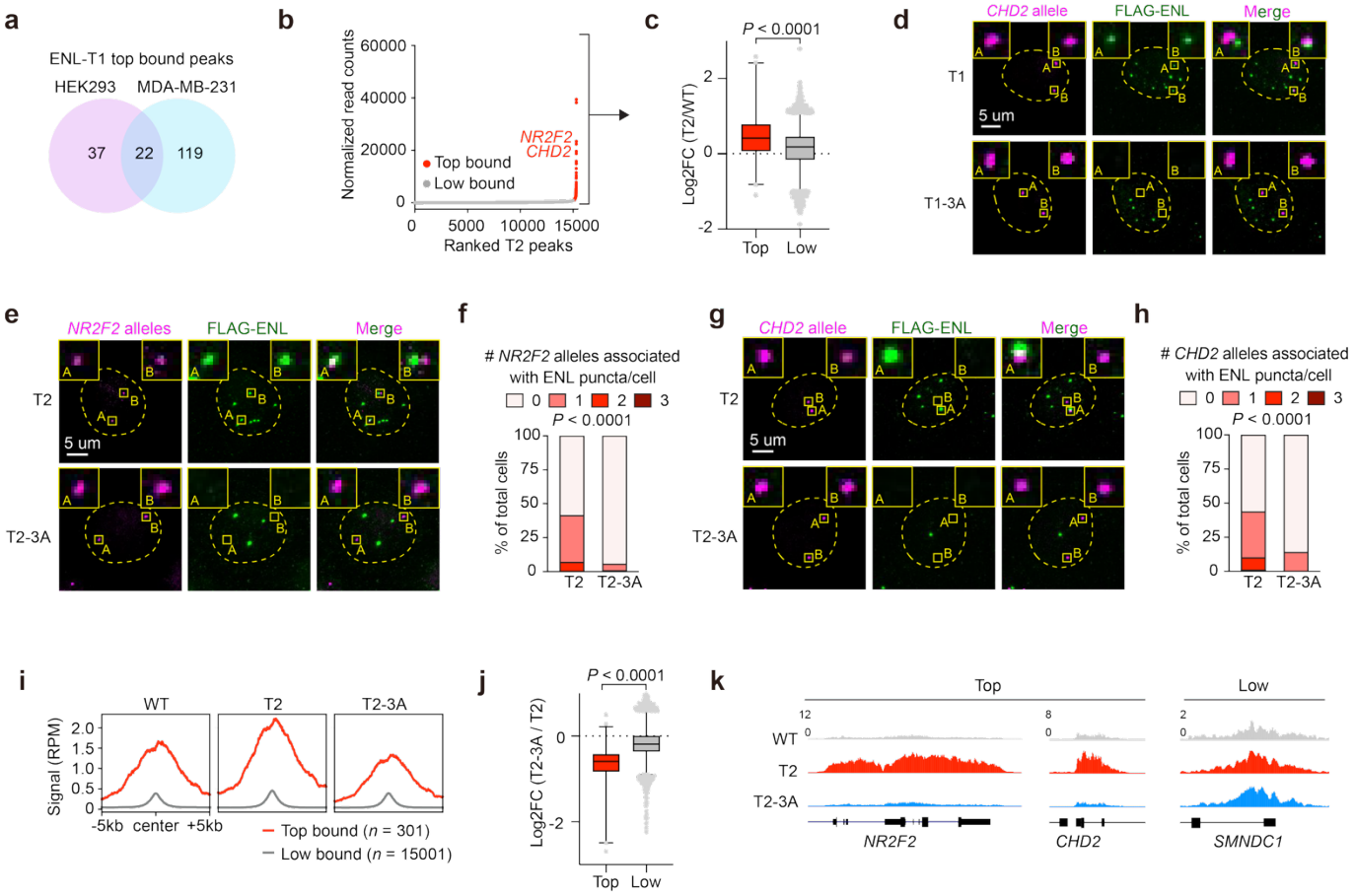

579 **Extended Data Fig. 7. RNA binding enhances mutant ENL occupancy at condensate-permissive**
580 **target loci in MDA-MB-231 cells. a,** Venn diagram showing shared or unique top-bound peaks in
581 HEK293 and MDA-MB-231 cells. **b,** ENL-T2 ChIP-seq peaks in MDA-MB-231 cells ranked by normalized
582 read count. Top-bound peaks fall to the right of the inflection point and are labeled in red text. Low-bound
583 peaks fall to the left of the inflection point and are labeled in gray. **c,** Box plot showing Log_2 fold change
584 of T2/WT signal at top or low-bound sites in MDA-MB-231. Top, n = 301; Low, n = 15,001. Center line
585 indicates median and box limits are set to 25th and 75th percentiles. P values were calculated by two-
586 tailed unpaired Student's t test. **d,** Representative *CHD2* DNA-FISH and FLAG-ENL IF staining in
587 HEK293 cells. Yellow dashed line outlines the nucleus. **e, g,** Representative *NR2F2* (**e**) or *CHD2* (**g**)
588 DNA-FISH and FLAG-ENL IF staining in MDA-MB-231 cells. Yellow dashed line outlines the nucleus. **f,**
589 **h,** Quantification of percentage of cells with indicated number of ENL puncta-associated *NR2F2* (**f**) or
590 *CHD2* (**h**) alleles. P values were calculated by two-tailed Fisher's exact test. **i,** Average chromatin
591 occupancy of ENL at top or low-bound sites in MDA-MB-231 cells. RPM, reads per million. **j,** Box plot
592 showing Log_2 fold change of T2-3A/T2 signal at top or low-bound sites in MDA-MB-231. Top, n = 301;
593 Low, n = 15,001. Center line indicates median and box limits are set to 25th and 75th percentiles. P values
594 were calculated by two-tailed unpaired Student's t test. **k,** Genome browser view of ENL ChIP signal at
595 representative top- and low-bound genes in MDA-MB-231 cells.

Extended Data Fig. 8

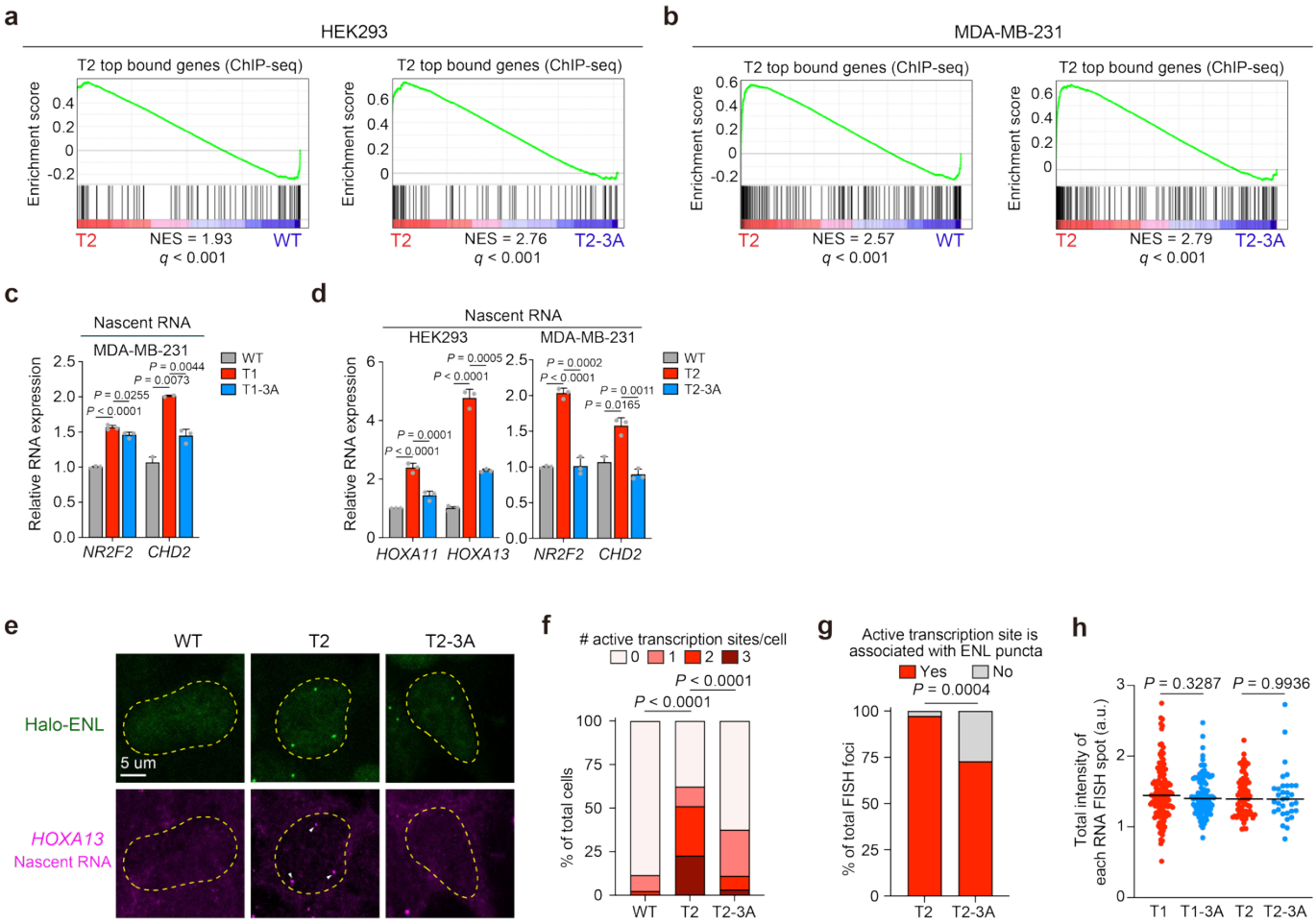

596 **Extended Data Fig. 8. RNA binding enhances transcriptional bursting and gene activation by**
597 **oncogenic ENL. a, b,** GSEA plots showing that top-bound genes (determined by ChIP-seq) are
598 upregulated in T2 versus WT or to T2-3A in HEK293 (**a**) and MDA-MB-231 (**b**) cells. NES, normalized
599 enrichment score. **c,** RT-qPCR showing nascent *NR2F2* or *CHD2* expression relative to *GAPDH* in MDA-
600 MB-231 cells expressing T1 variants. Data are mean ± s.d. *P* values were calculated by two-tailed
601 unpaired Student's t test. **d,** RT-qPCR showing nascent top target gene expression relative to *GAPDH* in
602 HEK293 or MDA-MB-231 cells expressing T2 variants. Data are mean ± s.d. *P* values were calculated by
603 two-tailed unpaired Student's t test. **e,** Nascent RNA-FISH for the *HOXA13* locus and Halo staining for
604 Halo-ENL in HEK293 cells. White arrows indicate RNA-FISH foci. Yellow dashed line outlines the
605 nucleus. **f,** Quantification of percentage of cells with indicated number of nascent RNA-FISH foci. *P*
606 values were calculated by two-tailed Fisher's exact test. **g,** Quantification of percentage of total *HOXA13*
607 RNA-FISH foci associated with ENL mutant puncta. *P* values were calculated by two-tailed Fisher's exact
608 test. **h,** Quantification of RNA FISH foci intensity (normalized to nuclear intensity). a.u., arbitrary units.
609 Horizontal line represents median. *P* values were calculated by two-tailed unpaired Student's t test.

Extended Data Fig. 9

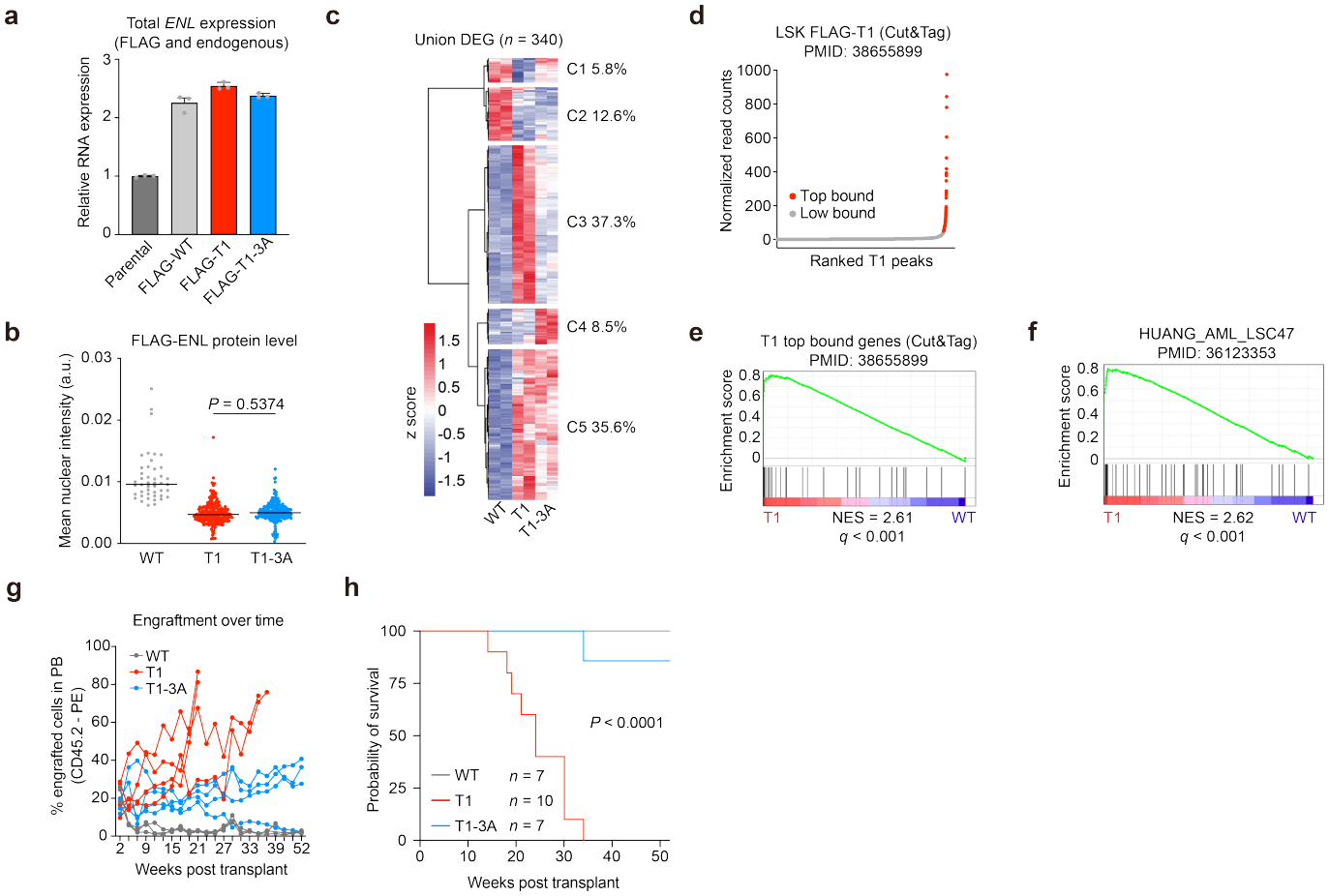

610 **Extended Data Fig. 9. Disrupting RNA binding impairs ENL mutant–driven leukemogenesis. a,** RT-
611 qPCR showing total human (transgene) and murine (endogenous) *ENL* RNA expression in transduced
612 LSK cells. **b,** Mean nuclear FLAG-ENL intensity in LSK cells represents relative protein expression. a.u.,
613 arbitrary units. Horizontal line represents median. *P* values were calculated using two-tailed unpaired
614 Student's t test. **c,** Heatmap depicting z-scores of all differentially expressed genes (DEGs). **d,** ENL-T1
615 ChIP-seq peaks in LSK cells ranked by normalized read count. Top-bound peaks fall to the right of the
616 inflection point and are labeled in red text. Low-bound peaks fall to the left of the inflection point and are
617 labeled in gray. **e,** GSEA plot showing that ENL-T1 top-bound genes are upregulated in T1 versus WT in
618 LSK cells. NES, normalized enrichment score. **f,** GSEA plot showing that genes associated with AML
619 patients (n = 47) are upregulated in T1 versus WT LSK cells. NES, normalized enrichment score. **g,**
620 Percentage of peripheral blood (PB) composed of cells derived from transplanted LSK. CD45.2,
621 leukocyte marker of donor LSK. **h,** Kaplan-Meier survival curves of mice receiving bone marrow
622 transplant. *P* value was calculated using Mantel-Cox log-rank test.

METHODS

Cell Lines

Reagent or Resource	Manufacturer/Source	Catalog Number
HEK293T	ATCC	CRL-3216
HEK293	ATCC	CRL-1573
WiT49	Laboratory of Herman Yeger	N/A
A549	Laboratory of Junwei Shi	N/A
MDA-MB-231	Laboratory of Yibin Kang	N/A

Antibodies

Reagent or Resource	Manufacturer	Catalog Number
Brilliant Violet 421™ anti-mouse CD3 Antibody	Biolegend	100227
Brilliant Violet 421™ anti-mouse CD19 Antibody	Biolegend	115549
Brilliant Violet 421™ anti-mouse/human CD11b Antibody	Biolegend	101251
Brilliant Violet 421™ anti-mouse/human CD45R/B220 Antibody	Biolegend	103240
Brilliant Violet 421™ anti-mouse TER-119/Erythroid Cells Antibody	Biolegend	116233
Brilliant Violet 421™ anti-mouse Ly-6G/Ly-6C (Gr-1) Antibody	Biolegend	108433
Brilliant Violet 421™ anti-mouse NK-1.1 Antibody	Biolegend	108741
Brilliant Violet 421™ anti-mouse CD11c Antibody	Biolegend	117343
Brilliant Violet 421™ anti-mouse TCR γ/δ Antibody	Biolegend	118119
Brilliant Violet 421™ anti-mouse TCR β chain Antibody	Biolegend	109229
PerCP/Cyanine5.5 anti-mouse Ly-6A/E (Sca-1)	Biolegend	108124
PE anti-mouse CD117 (c-Kit)	Biolegend	105808
CD45.1 mouse anti-mouse APC/Cy7	Fisher Scientific	BDB560579
CD45.2 mouse anti-mouse PE	Fisher Scientific	BDB560695
Flag	Sigma	F1804
MLLT1/ENL	Millipore Sigma	ABE2596
GAPDH	Cell Signaling Technology	2118
Anti-mouse IgG, HRP-linked Antibody	Cell Signaling Technology	7074S
Anti-rabbit IgG, HRP-linked Antibody	Cell Signaling Technology	7076S
Goat anti-Rabbit IgG (H+L) Cross-Adsorbed Secondary Antibody, Alexa Fluor 488	Invitrogen	A32731
Goat anti-Mouse IgG (H+L) Cross-Adsorbed Secondary Antibody, Alexa Fluor 488	Invitrogen	A32723
Goat anti-Rabbit IgG (H+L) Cross-Adsorbed Secondary Antibody, Alexa Fluor 568	Invitrogen	A-11036

Goat anti-Mouse IgG (H+L) Cross-Adsorbed Secondary Antibody, Alexa Fluor 568	Invitrogen	A11031
Goat anti-Rabbit IgG (H+L) Cross-Adsorbed Secondary Antibody, Alexa Fluor 647	Invitrogen	A-21245
Goat anti-Mouse IgG (H+L) Cross-Adsorbed Secondary Antibody, Alexa Fluor 647	Invitrogen	A-21236

Commercial Assays

Reagent or Resource	Manufacturer	Catalog Number
HisTrap HP His tag protein pur columns	Cytiva	29051021
Superdex 75 10/300 GL columns	Cytiva	28920504
Pierce microcentrifuge spin columns	Thermo Fisher	89879
RNA Clean & Concentrator Kit	Zymo Research	R1013
QIAquick PCR Purification Kit	Qiagen	28104
Vazyme Universal DNA Library Prep Kit for Illumina V4	Vazyme	ND610-04
Qubit 1X dsDNA High Sensitivity Kit	Invitrogen	Q33231
Agilent D1000 Screen Tape System	Agilent	N/A
RNeasy Mini Kit	Qiagen	74104
High-Capacity cDNA Reverse Transcription Kit	Applied Biosystems	4368814
NEBNext Poly(A) mRNA Magnetic Isolation Module	New England Biolabs	E7490L
NEBNext Ultra™ II RNA Library Prep Kit for Illumina	New England Biolabs	E7770L
NEBNext Multiplex Oligos for Illumina	New England Biolabs	E7335S
EasySep Mouse CD117 (cKIT) Positive Selection Kit	Stem Cell Technologies	18757

Media, chemicals, and other reagents

Reagent or Resource	Manufacturer	Catalog Number
DMEM with L-Glutamine, 4.5g/L Glucose and Sodium Pyruvate	Corning	MT10013CV
Eagle's Minimum Essential Medium (EMEM)	Corning	MT10009CV
DMEM/F-12	Sigma	D6421
IMDM + GlutaMAX	Gibco	31980030
Opti-MEM	Gibco	31985070
Hank’s Balanced Salt Solution (HBSS)	Gibco	14-170-112
Fetal Bovine Serum	Cytiva	SH103IH2540
Penicillin/Streptomycin	Gibco	15070063
Cycloheximide	Cell Signaling Technology	2112S
MethoCult	Stem Cell Technologies	03234
Recombinant murine Flt3 ligand	PeproTech	250-31L
Recombinant murine SCF	PeproTech	250-03
Recombinant murine TPO	PeproTech	315-14
Recombinant murine IL6	PeproTech	216-16
Recombinant murine IL3	PeproTech	200-03
RBC Lysis Buffer (10x)	BioLegend	420301
Zombie Aqua Fixable Viability Kit	BioLegend	423101

SYTOX Blue Dead Cell Stain	Invitrogen	S34857
2-Mercaptoethanol	BioRad	1610710
L-glutamine	Gibco	A2916801
PEI MAX	Polysciences	24765
Polyethylene Glycol 8000 (PEG)	Fisher Scientific	BP233-100
Polybrene	Millipore Sigma	TR-1003-G
Doxycycline	Sigma	D9891-1G
RetroNectin Recombinant Human Fibronectin Fragment	Takara Bio	T100B
Bovine Serum Albumin	Sigma Aldrich	A7906-10G
16% Paraformaldehyde Aqueous	Electron Microscopy Sciences	15710
Tween-20	Fisher Scientific	BP337500
Triton-X-100	Fisher Scientific	BP151500
Goat serum	Cell Signalling Technology	5425s
Mounting Medium with DAPI - Aqueous, Fluoroshield	Abcam	ab104139
PowerUp™ SYBR™ Green Master Mix for qPCR	Applied Biosystems	A25778
Glycine	Fisher Scientific	BP3815
Tris Base	Fisher Scientific	BP152-1
Blotting grade blocker	BioRad	1706404
SDS	Thermo Fisher	BP8200500
Pierce ECL Western Blotting Substrate	Thermo Scientific	32106
Tris-HCl	Fisher Scientific	BP153-500
EDTA	Sigma Aldrich	E5134-500G
NaDOC	Sigma Aldrich	35915
NaCl	Fisher Scientific	BP358-1
Sarkosyl	Sigma Aldrich	61739
DTT	Sigma Aldrich	D9163-5G
cOmplete EDTA-free Protease Inhibitor Cocktail	Sigma-Aldrich	11836170001
Dynabeads Protein A for IP	Invitrogen	10001D
LiCl	Sigma-Aldrich	213233-500G
NP-40	BioVision	2111-100
RNase A	Millipore Sigma	9001-99-4
Proteinase K	Thermo Scientific	EO0491
Poly-L-lysine solution	Sigma Aldrich	P8920
20X SSC buffer	Corning	46-020-CM
Formamide	Fisher Scientific	BP227-500
Dextran Sulfate	Sigma Aldrich	D8906
PVSA solution	Sigma Aldrich	278424
Hoechst 33342 solution, 20 mM	Thermo Scientific	62249
SlowFade Gold Antifade Mountant	Invitrogen	S36936
Glycerol	Fisher Scientific	P2291
RNase inhibitor (Murine)	Beyotime	R0102
10X TBE RNase-free	MREDA	M212499
APS	Sigma Aldrich	7727-54-0
TEMED	Sigma Aldrich	110-18-9
30%Arc-Bis RNase-free	Macklin	A917692
Imidazole	Sigma Aldrich	12399
D-Desthiobiotin	IBA Life Sciences	2-1000-002

Isopropyl β-D-1-thiogalactopyranoside	Sigma Aldrich	10724815001
Kanamycin	Fisher Scientific	BP906-5
Ni IDA Beads 6FF	Smart-Lifesciences	SA00501L
Strep-4FF beads	Smart-Lifesciences	SA053100
Alexa 488 Fluor™ 488 5-TFP	Invitrogen	A30005
HEPES-Na	Sigma-Aldrich	H7006
$H3_{34-28}$K27ac	This paper	SciLight Biotechnology, LLC
5' CY5 HOXA11 ssRNA 15nt/30nt	This paper	hippobio
5' CY5 HOXA11 ssDNA 15nt/30nt	This paper	xianghongbio
DEPC	Sigma-Aldrich	1609-47-8
BL21 (DE3) competent cells	Millipore Sigma	69450-3
HaloLink resin	Promega	G1913
Bovine serum albumin (BSA) fraction V	Sigma-Aldrich	126609-5GM
50X protease inhibitor cocktail	Promega	G6521
TURBO DNase	Invitrogen	AM2238
RNase Inhibitor, murine	New England Biolabs	M0314S
Ambion RNase I	Invitrogen	AM2294
FastAP Thermosensitive Alkaline Phosphatase	Thermo Scientific	EF0651
T4 Polynucleotide Kinase (PNK)	New England Biolabs	M0201S
T4 RNA ligase high concentration, T4 RNA ligase reaction buffer, 50% PEG8000, ATP	New England Biolabs	M0204
Dynabeads MyOne Silane	Invitrogen	37002D
Maxima H Minus Reverse Transcriptase	Thermo Scientific	EP0752
ExoI	New England Biolabs	M0293S
Instant Sticky-end Ligase Master Mix	New England Biolabs	M0370S
AMPure XP beads	Beckman Coulter	A63881
Janelia Fluor 657 (JF657)	Laboratory of Luke Lavis	N/A
Ribonucleoside vanadyl complexes (RVC)	Sigma Aldrich	R3380-5ML
Actinomycin D	Millipore Sigma	A9415-2MG
5,6-Dichlorobenzimidazole 1-β-D-ribofuranoside (DRB)	Millipore Sigma	D1916
Triptolide	Sigma	T3652-1MG
Alpha-Amanitin	Sigma	A2263-1MG

Recombinant DNA

Reagent or Resource	**Source**	**Catalog Number**
VSVG	Addgene	8454
PAX2	Addgene	12260
pCL-ECO	Addgene	12371
pLenti-tetON-miniCMV-3xFLAG-2xHA-hsENL-WT-NLS	Song *et al., Mol Cell,* 2022	N/A
pLenti-tetON-miniCMV-3xFLAG-2xHA-hsENL-T1-NLS	Song *et al., Mol Cell,* 2022	N/A
pLenti-tetON-miniCMV-3xFLAG-2xHA-hsENL-T1(K61A/R63A/K67A)-NLS ('T1-3A')	This paper	N/A
pLenti-tetON-miniCMV-3xFLAG-2xHA-hsENL-T2-NLS	Song *et al., Mol Cell,* 2022	N/A

pLenti-tetON-miniCMV-3xFLAG-2xHA-hsENL-T2(K61A/R63A/K67A)-NLS ('T2-3A')	This paper	N/A
pLenti-tetON-miniCMV-Halo-3xFLAG-hsENL-WT-NLS	Song *et al., Mol Cell,* 2022	N/A
pLenti-tetON-miniCMV-Halo-3xFLAG-hsENL-T1-NLS	Song *et al., Mol Cell,* 2022	N/A
pLenti-tetON-miniCMV-Halo-3xFLAG-hsENL-T1(K61A/R63A/K67A)-NLS ('T1-3A')	This paper	N/A
pLenti-tetON-miniCMV-Halo-3xFLAG-hsENL-T2-NLS	Song *et al., Mol Cell,* 2022	N/A
pLenti-tetON-miniCMV-Halo-3xFLAG-hsENL-T2(K61A/R63A/K67A)-NLS ('T2-3A')	This paper	N/A
MSCV-3xFLAG-HA-hsENL-WT-PGK-puro-IRES-GFP	Liu *et al., Cancer Discov,* 2024	N/A
MSCV-3xFLAG-HA-hsENL-T1-PGK-puro-IRES-GFP	Liu *et al., Cancer Discov,* 2024	N/A
MSCV-3xFLAG-HA-hsENL-T1(K61A/R63A/K67A)-PGK-puro-IRES-GFP	This paper	N/A
pET28a-2*strep-ENL-WT-6*his	Song *et al., Mol Cell,* 2022	N/A
pET28a-2*strep-ENL-T1-6*his	Song *et al., Mol Cell,* 2022	N/A
pET28a-2*strep-ENL-T1(K61A/R63A/K67A)-6*his	This paper	N/A
pET28a-6*his-ENL-WT(1-148)	Song *et al., Mol Cell,* 2022	N/A
pET28a-6*his-ENL-T1(1-151)	Song *et al., Mol Cell,* 2022	N/A
pET28a-6*his-ENL-T1(K61A/R63A/K67A)(1-151)	This paper	N/A

Software and algorithms

Reagent or Resource	**Manufacturer**	**Catalog Number**
FIJI	Schindelin *et al.,* 2012	imagej.net/software/fiji/
GraphPad Prism	GraphPad	graphpad.com
Imaris 9.3.1	Oxford Instruments	imaris.oxinst.com
Origin 7.0	OriginLab	originlab.com
PyMOL 3.1	PyMOL	pymol.org
Alphafold3 Server	N/A	PMID: 38718835
FlowJo	BD Biosciences	flowjo.com
GSEA_4.3.2	N/A	PMID: 16199517; PMID: 12808457

Protein purification

For full-length ENL protein purification, N-terminal 2 X streptavidin tags and C-terminal 6 X histidine tags were added to the pET28b expression vector containing the ENL-WT CDS (residues 1-559; NP_005925.2). The T1 mutation (p. 117_118insNHL) and RNA-binding residue mutations (K61A, R63A, and K67A) were subsequently added. Proteins were expressed in BL21(DE3) *E. coli* cells induced with 0.4mM IPTG (Isopropyl β-D-thiogalactopyranoside) for 16 h at 16°C. Cells were harvested and resuspended in lysis buffer (25 mM Tris-HCl pH 7.5, 500 mM NaCl, 5% glycerol, 50 mM imidazole, 1 mM PMSF). After lysis using an Emulsiflex C3 (Avestin) high-pressure homogenizer, crude lysate was clarified by centrifugation. Clarified lysate was loaded onto a HisTrap column and washed with wash buffer (30 mM Tris-HCl pH 7.5, 1 M NaCl, 5% glycerol). Protein was eluted using lysis buffer supplemented with 500 mM

633 Imidazole, concentrated, and buffer-exchanged to strep buffer (25 mM HEPES-Na pH 7.4, 500 mM NaCl,
634 5% glycerol, 1 mM EDTA, 2 mM β-mercaptoethanol) to decrease the imidazole concentration. After buffer
635 exchange, the protein was incubated with strep-4FF beads, washed with strep buffer, and eluted using
636 strep buffer supplemented with 5 mM desthiobiotin.
637
638 For purification of the ENL YEATS (residues 1-148) domain, N-terminal 6 X histidine tags were added to
639 the pET28b vector containing the ENL-WT YEATS domain CDS (residues 1-148). The T1 mutation (p.
640 117_118insNHL) and RNA-binding residue mutations (K61A, R63A, and K67A) were subsequently added.
641 Proteins were expressed in BL21(DE3) *E. coli* cells induced with 0.4mM IPTG for 16h at 16°C. Cells were
642 harvested and resuspended in lysis buffer. After lysis using an Emulsiflex C3 high-pressure homogenizer,
643 crude lysate was clarified by centrifugation. Clarified lysate was loaded onto a HisTrap column and washed
644 with wash buffer (30 mM Tris-HCl pH 7.5, 1 M NaCl, 5% glycerol). Protein was eluted with a linear imidazole
645 gradient from 20 mM to 500 mM. Protein was further purified and polished over a Superdex 75 10/300 gel
646 filtration column using AKTA Purifier 10 systems (GE Healthcare). The monomer peak in elution buffer
647 (500 mM NaCl, 25 mM Tris-HCl pH 7.5, and 2 mM β-mercaptoethanol) was pooled, concentrated to about
648 10 mg/mL, and stored at −80°C.
649
650 **AlphaFold predictions and analysis**
651 We used the Alphafold-Multimer (v3) to predict the structure of the ENL YEATS-RNA complex. The human
652 ENL 1-142 T1 sequence was submitted as the protein sequence, and the first 15 nucleotides of 104
653 randomly selected transcripts were chosen as input RNA sequences (Supplementary Table 1). Each model
654 was predicted using one ENL YEATS domain and one RNA fragment. For all predicted results, the top-
655 scoring relaxed model was selected, with an average iPTM score > 0.6 being inferred as putative hits.
656 Diagnostic plots (PAE plot, PLDDT plot, and sequence coverage) and generated structures were manually
657 checked. The regions characterizing the interaction between ENL and RNA were extracted from the PAE
658 matrix, and the minimum PAE corresponding to each ENL residue was calculated and normalized. The
659 PAE values corresponding to each residue were summed and mapped onto the structure for visualization.
660
661 To examine the impact of the 3A mutation on ENL:RNA interactions, we performed the same Alphafold
662 modelling with the T1-3A YEATS domain sequence and the 104 RNA sequences. For the 104 T1:RNA
663 models and 104 T1-3A:RNA models, we measured the shortest possible distance between each of ENL's
664 putative RNA binding residues (K61, R63, and K67) and the RNA molecule. We then plotted the percentage
665 of models that show each individual residue as being within 3, 4, or 5 Å of the RNA molecule.
666
667 **Electrophoretic mobility shift assay (EMSA)**
668 The nucleic acids used in the experiment were all 5' cy5 labeled. ssRNA was first incubated at 95°C for 5
669 minutes and then quickly cooled on ice for 5 minutes. RNA refolding buffer (10 mM Bis-Tris pH 6.7, 50 mM
670 KCl, 10 mM $MgCl_2$; 1X final) was then added to the RNA on ice. To refold, the RNA was transferred to a
671 cold metal block and folded by warming to room temperature (~25°C) for 30 minutes. For dsDNA, the cy5
672 labeled DNA oligo was mixed with an equal amount of unlabeled complementary oligo in DNA annealing
673 buffer (10 mM Tris-HCl pH 8.0, 50 mM NaCl, 1 mM EDTA,1 X final), heated at 90°C for 3 minutes, and
674 then cooled slowly to room temperature. The prepared nucleic acids were incubated with purified ENL
675 protein in RNase-free ultra-low adhesion PCR tubes. The reactions contained 1 X binding buffer (1x PBS
676 with 5% glycerol, 2 mM β-ME, and 0.4 U/μL Murine RNase inhibitor (Beyotime)). The reactions were loaded
677 on a 6% native polyacrylamide gel (29:1 Acrylamide: Bis-acrylamide) and electrophoresed at 100 V for 1
678 hour in 0.5x TBE. The gel was imaged and photographed using a Tanon gel imaging system with a 605
679 nm light source. The experiment was performed with at least three technical replicates and three biological
680 replicates. All reagents and equipment used in the experiment were RNase-free.
681
682 ***In vitro* droplet formation assay**
683 Droplet formation assay was performed in the droplet formation buffer (1X PBS with 5% glycerol and 2 mM
684 β-ME). Proteins were fluorescently labeled for microscopy using Microscale Protein Labeling kits from
685 Thermo Scientific: Alexa Fluor 488 (A30005). Synthetic nucleic acids labeled with 5' cy5 were used in the
686 experiment. Labeled proteins were added to unlabeled proteins at a 1:10 molar ratio. Droplets were

assembled in 384 low-binding multi-well 0.17-mm microscopy plates (384-well microscopy plates) (In Vitro Scientific) and sealed with optically clear adhesive film. For the groups with RNase treatment, RNase A powder is pre-dissolved in droplet formation buffer. After ENL and RNA have been incubated in droplet formation buffer, RNase A is added to achieve a final concentration of 1 μg/mL and incubated at room temperature for 5 minutes. All reagents used in the experiment were RNase-free. After quick centrifugation, droplets were imaged under Olympus FV1200 using a 100 X oil objective. The results were processed by Imaris 9.3.1 (Oxford Instrument). Total droplet area was defined by and plotted as the total area of a field occupied by droplets. Total RNA signal per droplet is defined by the sum of RNA channel pixel intensities within a mask drawn over each individual droplet.

Isothermal titration calorimetry (ITC)

All ITC titrations were performed at 25°C using MicroCal iTC200 system (Malvern). Both synthetic histone H3 peptides ($H3_{24-28}$K27ac) and the recombinant ENL YEATS domain proteins were extensively dialyzed against ITC buffer (25 mM Tris-HCl pH 7.5, 500 mM NaCl, 5 % glycerol and 2 mM β-ME). Before titration, all samples were centrifuged at 13,000 rpm at 4°C for ~10-15 minutes to remove potential aggregates. ITC cells were rinsed with buffer for several times before protein solution was added to the cell. Cell contents were pipetted several times to mix with any trace buffer remaining in the cell. A small volume of protein solution was removed from the cell for concentration re-check using a NanoDrop. Each ITC titration consisted of 17 successive injections with 0.5 μL for the first and 2.4 μL for the rest. The intervals between injections were 150 seconds, and the stirring speed was 750 rpm. Histone H3 peptides (2.0-2.2 mM) were titrated into ENL YEATS domain proteins (0.15 mM) in all experiments. The resultant ITC curves were processed using the Origin (v.7.0) software (OriginLab) in accordance with the “One Set of Sites” fitting model. First injection data was always excluded from the analysis.

Human cell lines

All cell lines used in this study were cultured in a humidified incubator maintained at 37°C and 5% CO_2 and regularly tested mycoplasma negative. All cell lines not purchased from ATCC were subjected to STR authentication testing prior to any experimentation. HEK293T, A549, MDA-MB-231 were cultured in DMEM supplemented with 10% FBS and 100 U/mL penicillin/streptomycin. HEK293 cells were cultured in EMEM supplemented with 10% FBS and 100 U/mL penicillin/streptomycin. WiT49 cells were cultured in DMEM/F-12 supplemented with 10% FBS and 100 U/mL penicillin/streptomycin.

Lentivirus and retrovirus generation

HEK293T cells were used for all virus packaging. For lentivirus generation, cells were seeded 1 day prior to transfection. For transfection, lentiviral packaging plasmids VSVG and PAX2 were combined with the plasmid of interest and Polyethylenimine MAX (PEI MAX) in Opti-MEM at a ratio of 1:4, total DNA (ug): PEI (uL). These components were incubated to allow for complex formation and added to the HEK293T cells. ~6h after adding the mix, transfection media was removed and replaced with fresh culture media. The next day, virus was collected and fresh culture media was added back to the cells. A total of 5 virus collections occurred over the course of 72h post-transfection. For retrovirus generation, cells were seeded 1 day prior to transfection. For transfection, retrovirual packaging plasmid pCL-ECO was combined with the plasmid of interest and Polyethylenimine MAX (PEI MAX) in Opti-MEM at a ratio of 1:3, total DNA (ug): PEI (uL). These components were incubated to allow for complex formation and added to the HEK293T cells. ~6h after adding the mix, transfection media was removed and replaced with fresh culture media. The next day, virus was collected and fresh culture media was added back to the cells. A total of 5 virus collections occurred over the course of 72h post-transfection. When necessary, virus was concentrated 100x with 5x PEG8000 solution.

Human cell line viral transduction and transgene expression

HEK293 and WiT49 stable cell lines were generated by incubating cells (~70% confluent) with concentrated lentivirus and 10 ug/mL polybrene overnight (~16h). A549 and MDA-231 stable cell lines were generated by adding concentrated lentivirus and 10 ug/mL polybrene to cells (~70% confluent), performing spinfection (2500 rpm for 1h), and incubating overnight. When applicable, selection regents were added 24-48 hours post-infection. Cells containing doxycycline-inducible transgenes (i.e., ENL) were

741 incubated for 48h with a pre-determined concentration of doxycycline such that exogenous ENL expression
742 was similar to that of endogenous ENL as measured by protein levels in Western blot.
743
744 **CLAP pull-down and RNA isolation**
745 CLAP-sequencing was conducted according to published protocols from the Dr. Mitchell Guttman lab[34]
746 with some modifications. For CLAP experiments, HEK293 cells stably expressing doxycycline-inducible
747 Halo-tagged ENL transgenes were used (~50-60M cells used per replicate per condition). Cells were
748 treated with pre-determined concentrations of doxycycline for 48h prior to experimentation. Plates of
749 adhered cells were UV crosslinked in PBS on ice at an energy setting of 400 mJ/cm^2. Immediately following
750 crosslinking, cells were harvested, washed with ice cold PBS, centrifuged, and stored as cell pellets at -
751 80°C.
752
753 Prior to performing pull-down, HaloLink resin was washed three times in PBST (PBS + 0.1% Tween-20)
754 and blocked in 1% nuclease-free BSA (fraction V) for 20 minutes at room temperature. Resins were then
755 washed three more times in PBST. Crosslinked cell pellets were incubated for 10 minutes on ice in lysis
756 buffer (RIPA buffer (1M HEPES pH 7.4, 5M NaCl, 10% deoxycholate, 20% SDS, 10% NP-40), 1X Promega
757 protease inhibitor cocktail, 1X TURBO DNase, 1x Mn^{2+}/Ca^{2+} mix (1M $MnCl_2$, 1M $CaCl_2$), and Murine RNase
758 inhibitor). Lysates were transferred to 1mL Bioruptor sonication tubes and sonicated on the "low setting"
759 for 5 minutes (30s on/30s off) at 4°C. Following sonication, TURBO DNase and diluted RNase I (1:25 in
760 PBS) were added to lysates and incubated at 37°C for 5 minutes with shaking at 1200 rpm. Immediately
761 then murine RNase inhibitor was added to quench the reaction and lysates were then centrifuged at 15,000
762 rcf for 10 minutes at 4°C. ~5% of the supernatant was reserved in -80°C to use later as an input control.
763 The remaining lysate was added to the prepared HaloLink resin and incubated at 4°C overnight with
764 rotation.
765
766 The next day, the following five CLAP wash buffers were prepared fresh and pre-warmed to 80°C prior to
767 use: CLAP wash buffer 1 (20% N-lauroylsarcosine, 500mM EDTA, PBS); CLAP wash buffer 2 (1M HEPES
768 pH 7.4, 5M NaCl, 10% NP-40, water); CLAP wash buffer 3 (1M HEPES pH7.4, 10% NP-40, 8M urea);
769 CLAP wash buffer 4 (1M HEPES pH 7.4, 10% NP-40, 10% Tween-20, water); CLAP wash buffer 5 (1M
770 HEPES pH 7.4, 10% NP-40, 500mM EDTA, water). Overnight captures were centrifuged and supernatants
771 were discarded. Resins were washed twice with RIPA buffer. Resins were then washed three times each
772 with each CLAP wash buffer in numerical order. For each wash, buffer was added to resins and incubated
773 at 90°C for 3 minutes with shaking at 1200 rpm before centrifugation and removal of supernatant. Final
774 resin pellets, as well as the reserved input samples, were then subjected to proteinase K elution by
775 incubating with CLAP wash buffer 1 and proteinase K at 50°C for 20 minutes with shaking at 1200 rpm.
776 The slurry was then transferred to Pierce micro-centrifuged columns to remove the resin. Supernatants
777 were then used for RNA extraction with the Zymo RNA clean and concentrator kit. Eluted RNA was used
778 for subsequent library preparation.
779
780 **CLAP library preparation**
781 Input samples were first incubated with 1x TURBO DNase buffer and TURBO DNase at 37°C for 15
782 minutes with shaking at 1200 rpm and subsequently subjected to RNA purification again using the Zymo
783 clean and concentrator kit. Eluted input RNA was then mixed with 1X FastAP buffer, fragmented at 91°C
784 for 90s, and incubated with FastAP enzyme and murine RNase inhibitor for 10 minutes at 37°C with
785 shaking at 1200rpm. At the same time, CLAP samples were mixed with 1X FastAP buffer, FastAP enzyme,
786 TURBO DNase, and murine RNase inhibitor, and incubated for 10 minutes at 37°C with shaking at
787 1200rpm. Then, for all input and CLAP samples, PNK mix (1X PNK buffer, PNK enzyme, TURBO DNase)
788 was added on top of the FastAP reaction and incubated for an additional 10 minutes at 37°C with shaking
789 at 1200rpm. RNA was then purified using the Zymo RNA clean and concentrator kit.
790
791 To each sample, we then added the RIL19 adaptor (5'–
792 /Phosphate/rArGrArUrCrGrGrArArGrArGrCrGrUrCrGrUrG/3ddC/ – 3') in DMSO and incubated at 65°C for
793 2 minutes. Then ligation mix (1X T4 RNA ligase buffer, ATP, PEG8000, murine RNase inhibitor, and T4

RNA ligase high concentration) was added and incubated at room temperature for 1 hour and 15 minutes with rotation. Adaptor-ligated RNA was then cleaned with SILANE beads.

Eluted RNA was then incubated with reverse transcription adaptor AR17 (5'-ACACGACGCTCTTCCGA-3') at 65°C for 2 minutes. Reverse transcription mix (1X Maxima RT buffer, dNTPs, murine RNase inhibitor, Maxima RT enzyme) was added to the adaptor ligated RNA and incubated at 50°C for 20 minutes. Samples were then incubated with ExoI at 37°C for 15 minutes and quenched with EDTA on ice. To fragment RNA, the samples were incubated with NaOH at 80°C for 6 minutes and neutralized with equal amount of HCl. Reverse transcription product was then cleaned with SILANE beads. The resulting cDNA was then mixed with a splint adaptor (detailed in the published protocol) and 1X Instant Sticky Master Mix and incubated for 4 hours at room temperature with shaking at 1000 rpm. Each reaction was then cleaned with SILANE beads.

With the eluted cDNA samples we then performed PCR with NEBNext Universal primers for Illumina, NEBNext Index primers for Illumina, and 1X Q5 master mix. The following PCR conditions were used: (1X) 98°C 1 minute; (4X) 98°C 15s, 69°C 15s, 72°C 90s; (4X for inputs, 10X for IP) 98°C 15s, 72°C 90s; (1X) 72°C 2 min). PCR products then underwent 1.2X SPRI bead size selection and elution. Concentrations of the final barcoded libraries were measured on the Qubit and size measurements were calculated using the Agilent Tapestation prior to sequencing on a NextSeq2000.

CLAP-seq data processing and analysis

The mapping of CLAP-sequencing was conducted according to published protocols from the Dr. Mitchell Guttman lab[34]. Adapters were trimmed from the paired end sequencing reads using cutadapt v4.9 from Trim Galore!. The RNA alignment was performed in two parts. First, the reads were aligned to hg38 genome reference containing both repetitive and structure RNAs using bowtie2. Second, the remaining reads were recycled and aligned to hg38 with STAR. After alignment, MarkDuplicates function from the Picard package was used to remove any PCR duplications. Finally, alignments from both mapping methods were finally merged into a single bam file for future analysis. CLAP peaks were identified by MACS2 peakcalling with IP and input from each condition using macs2 callpeak -t -c -f BAMPE -g hs -n --nomodel --broad --broad-cutoff 1e-10 -p 1e-10 --keep-dup all. Peak distribution and associated genes were identified using HOMER module annotatePeaks.pl v4.11. NGS plots were generated use ngs.plot.r v2.61.

Western blot

Cells were collected, washed once in PBS, and boiled (95°C) in 1X SDS loading buffer (5X SDS loading buffer: 0.25M Tris-HCl (PH6.8), 0.5M DTT, 10% SDS, 50% glycerol, 0.25% BPB, 1% b-mercaptoethanol (b-ME) for 20 minutes. Lysates were run on homemade 10% SDS-PAGE gels in homemade 1X running buffer (2.5mM Tris Base, 19.2 mM Glycine, 0.01% SDS in H2O, pH 8.3). Protein was transferred to PVDF membrane (Millipore, 0.45 um) using freshly made homemade transfer buffer (1.2 mM Tris Base, 9.6 mM Glycine in H2O, pH 8.3) + 20% methanol on ice. After transferring, membranes were blocked with 5% blocking buffer in PBST (PBS + 0.1% Tween) for 45 minutes at room temperature. Membranes were then incubated with primary antibody suspended in 1% blocking buffer overnight at 4°C with rocking. The next day, membranes were washed three times for 10 minutes each wash with PBST. Membranes were then incubated with secondary antibody suspended in 1% blocking buffer for 1 hour at room temperature and subsequently washed three more times in PBST as before. Blots were covered with Pierce ECL Western Blotting Substrate according to the manufacturer's instructions and imaged using film. Primary antibodies were diluted as follows: Flag (1:1000), MLLT1/ENL (1:1000), GAPDH (1:5000). Secondary antibodies were used as follows: Anti-mouse or Anti-rabbit IgG HRP-linked (1:2500).

Cycloheximide pulse chase

HEK293 cells expressing Flag-tagged ENL transgenes were incubated with doxycycline for 48h prior to experimentation. Cells were treated with 50 ug/mL cycloheximide for and collected at indicated timepoints. The intensity of each sample's ENL blot was normalized to the intensity of that sample's GAPDH blot. Intensities were measured in FIJI.

848 **Immunofluorescence staining and confocal microscopy**
849 Cells (150K/well) were seeded on 24-well plates containing coverslips and incubated 24-48h. Cells were
850 fixed with 4% PFA in PBS for 10 min at room temperature, washed with PBST (PBS + 0.1% Tween-20)
851 three times (5 min/wash), and then permeabilized with PBS containing 0.1% Triton-X 100 for 10 min, and
852 washed three times with PBST as before. Subsequently, cells were blocked in PBS with 10% goat serum
853 for 30 min at room temperature. Cells were then incubated overnight at 4°C with primary antibodies (1:300)
854 in 1% BSA in PBS. The next day, cells were washed three times in PBST, incubated with secondary Alexa
855 Fluor-conjugated antibodies (1:250) in 1% BSA for 1h at room temperature, and washed three more times
856 in PBST. The coverslips were then mounted face down on slides in DAPI-containing mounting medium.
857 Primary antibodies used: Flag (Sigma F1804) and MLLT1/ENL (Millipore ABE2596). Secondary antibodies
858 used: goat anti-Rabbit or anti-Mouse IgG (H+L) conjugated with Alexa Fluor 488, 568, or 647 (Invitrogen).
859 Images were captured on Zeiss LSM880 or Leica Stellaris 5 confocal microscopes.
860
861 **DNA-FISH with immunofluorescence staining**
862 Poly-L-lysine was first added to wells of rubber gaskets adhered to glass microscopy slides and
863 removed/dried prior to cell plating. Cells were then plated in the gasket wells and allowed to adhere at
864 37°C for 1.5-2h (HEK293 and MDA-MB-231cells) or 20 minutes (LSK cells). Slides were then fixed in 4%
865 PFA for 10 minutes at room temperature in coplin jars followed by three 10 minute washes in room
866 temperature (RT) PBS. **DNA-FISH Part 1**: Slides were permeabilized in 0.5% Triton-X-100 in PBS for 15
867 minutes at RT and washed once in PBS for 5 minutes at RT. Next slides were incubated in 70% EtOH,
868 90% EtOH, and 100% EtOH for 2 minutes each time. Slides were then washed once in 2X SSCT (1X SSC
869 + 0.1% Tween-20) for 5 minutes at RT and incubated once in 70% FMM buffer (70% formamide, 1X SSC,
870 water) for 5 minutes at RT. Slides were then transferred to 70% FMM buffer pre-heated to 37°C for 1 h.
871 Then primary FISH probe hybridization solution (50pmol primary probe, 100uM dNTP, 50% FMM, 1X
872 dextran-sulfate PVSA hybridization mix, 10ug RNase A, water) was added to each slide, sealed with a
873 coverslip and rubber cement, and denatured on a water-immersed heat block for 30 minutes at 83°C.
874 Slides were then transferred to a humidity chamber and incubated overnight at 37°C. **DNA-FISH Part 2:**
875 The next day, slides were washed once in 2X SSCT for 10 minutes at 60°C, once in 2X SSCT for 10
876 minutes at RT, and once in 0.2X SSC for 10 minutes at RT. Slides were then incubated with secondary
877 FISH probe for 2 h at RT protected from light under coverslips sealed with rubber cement (secondary probe
878 mix: 10pmol secondary probe, 10% FMM, 1X dextran-sulfate PVSA hybridization mix, water). Slides were
879 then washed again in 2X SSCT 60°C, 2X SSCT RT, and 0.2X SSC as before. **IF Part 1:** Slides were next
880 fixed again in 2% PFA for 10 minutes at RT, washed once in PBS for 5 minutes at RT, permeabilized with
881 0.1% Triton-X-100 for 15 minutes at RT, and washed three times in PBST (PBS + 0.1% Tween-20) for 10
882 minutes each at RT. Slides were then blocked in 1% BSA in PBST for 45 minutes at RT. Then primary
883 antibody solution (1:300 primary antibody in 1% BSA) was added to each slide, sealed with a coverslip
884 and rubber cement, and incubated overnight at 4°C in a humidity chamber. **IF Part 2:** The next day, slides
885 were washed three times in PBST for 10 minutes each time. Then secondary antibody solution (1:250
886 secondary antibody in 1% BSA) was added to each slide, sealed with a coverslip and rubber cement, and
887 incubated for 2 h at RT. Slides were washed again three times in PBST for 10 minutes each time. Finally,
888 slides were incubated in DAPI staining buffer (2X SSC + 1:10,000 Hoescht stain) for 5 minutes at RT and
889 washed once in PBS for 5 minutes at RT. Coverslips were added to each slide with anti-fade mounting
890 media and sealed with clear nail polish.
891
892 Primary probes used: Probes were designed to cover ~100kb regions (4 40mer probes per kb) of the
893 human *HOXA9-13* locus, human *CBX3* locus, human *NR2F2* locus, human *CHD2* locus, mouse *Hoxa9-*
894 *10* locus, or mouse *Meis1* locus. Secondary probes were dye conjugated. Primary antibodies used: Flag
895 for HEK293 and MDA-MB-231 cells (Sigma F1804) and MLLT1/ENL (Millipore ABE2596) for LSK cells.
896 Secondary antibodies used: goat anti-Rabbit or anti-Mouse IgG (H+L) conjugated with Alexa Fluor 488,
897 568, or 647 (Invitrogen). Images were captured on Zeiss LSM880 or Leica Stellaris 5 confocal
898 microscopes.
899
900 **ChIP-qPCR and ChIP-sequencing**

Between 20-25M cells were used per ChIP. Cells were collected from plates and fixed in freshly made 1% PFA in PBS (1mL 1% PFA per 10M cells). For Flag ChIP, fixation was performed for 10 minutes at room temperature with intermittent inversion. PFA was quenched with 125mM Glycine for 5 minutes at room temperature and the cell pellet was then washed three times with PBS. Cells were then resuspended in RIPA3.0 buffer (0.1% SDS, 1% Triton-X-100, 10mM Tris-HCl pH7.4, 1mM EDTA pH8, 0.1% NaDOC, 0.3M NaCl) freshly supplemented with 1/40 volume of 10% sarkosyl, 1mM DTT, and protease inhibitor. For MDA-MB-231 ChIPs, an extra 0.1% SDS (final 0.2% total) was added to the sonication buffer to improve sonication. Cells were sonicated on a Covaris Ultrasonicator. Concurrently, primary antibody was incubated with Protein A Dynabeads and then washed three times with PBS + 0.1% Tween-20. A small volume of sonicated lysate was reserved as an input control. Remaining lysate was rotated overnight at 4°C with the primary antibody-bound Dynabeads. For MDA-MB-231 ChIPs, sonicated lysates (which contain extra SDS in the sonication buffer) were diluted with non-SDS containing sonication buffer to a final concentration of 0.1% SDS before adding to the antibody-bound beads. While extra SDS improved sonication, this SDS can interfere with IP and must be re-diluted before IP. The next day, beads were washed three times with low salt buffer (150mM NaCl, 0.1% SDS, 1% Triton-X-100, 1mM EDTA pH8, 50mM Tris-HCl pH8), three times with high salt buffer (500mM NaCl, 0.1% SDS, 1% Triton-X-100, 1mM EDTA pH8, 50mM Tris-HCl pH8), and three times with LiCl buffer (150mM LiCl, 0.5% NaDOC, 0.1% SDS, 1% NP-40, 1mM EDTA pH8, 50mM Tris-HCl). Beads were then washed once with TE buffer (1mM EDTA, 10mM Tris-HCl pH8) + 50mM NaCl. Elution buffer (1% SDS, 50mM Tris-HCl ph8, 10mM EDTA, 200mM NaCl) was then added to the beads and incubated at 65°C with shaking for 0.5h. Beads were then centrifuged and supernatant was transferred to a new tube and incubated overnight at 65°C. At this point elution buffer was also added to reserved input lysate and incubated overnight at 65°C. The next day, the samples were first incubated with RNase A for 1h and 37°C and then with Proteinase K for 1h at 55°C. DNA was purified using the Qiagen PCR purification kit and eluted in PCR water.

For qPCR, ChIP DNA was diluted 50x in water and qPCR was performed using SYBR green master mix. Primers used are listed in Supplementary Table 11. For ChIP-sequencing, ChIP DNA was subjected to library preparation using the Vazyme Universal DNA Library Prep Kit for Illumina. Prior to sequencing, libraries were quantified and size confirmed using the Qubit and Tapestation according to the manufacturers' instructions. Final libraries were sequenced on an Illumina Nextseq 2000.

Reads were aligned to the human reference genome (hg19) by the package Bowtie2 v2.5.4 with the default parameters. The package samtools v1.9 was used for converting to BAM format, sort- ing, removing duplicates, and indexing. In ChIP-seq analysis, we utilized the corresponding input data as a control during peak calling. The chromatin distribution of the peaks was determined by HOMER module annotatePeaks.pl v 4.11. Peaks are listed in Supplementary Tables 2, 4). To make the heatmaps, the filtered, sorted, and indexed BAM files were converted to bigwig files using the bamCoverage from deeptools v3.5.6 and then normalized by counts per million (CPM). Heatmaps were generated using the module computeMatrix and plotHeatmap from deeptools v3.5.6.

RNA extraction, cDNA synthesis, and RT-qPCR

Total RNA was extracted using Qiagen RNeasy kits according to the manufacturer's instructions. Reverse transcription was performed using the High-Capacity cDNA Reverse Transcription Kit (Applied Biosystems) according to the manufacturer's protocol. Quantitative real-time PCR was performed using SYBR green master mix. Primers used are listed in Supplementary Table 11.

RNA-sequencing and Gene Set Enrichment Analysis (GSEA)

RNA was extracted as described above. Library preparation was performed with 500 ng total RNA beginning with the NEB polyA mRNA magnetic isolation module followed by NEB library preparation kit, both according to the manufacturer's instructions. Prior to sequencing, libraries were quantified and size confirmed using the Qubit and Tapestation according to the manufacturers' instructions. Final libraries were sequenced on an Illumina Nextseq 2000.

954 Reads were aligned to the mouse reference genome (mm10) using HISAT2 v 2.2.1 with default
955 parameters. The package featureCounts v2.0.2 was used for counting the mapped reads in each mouse
956 gene. Transcript per million (TPM) was used for normalizing the gene expression. Differentially expressed
957 genes between conditions were statistically determined by R package DESeq2 v1.38.3. Genes with
958 adjusted *P* value < 0.05 and fold change ≥ 1.5 were reported as differential genes. Differentially expressed
959 genes in LSK are listed in Supplementary Table 9.
960
961 For gene set enrichment analysis, custom gene signatures were made from our ChIP-sequencing datasets
962 (Supplementary Tables 5, 6, 8). Briefly, normalized read counts for ENL-T1 or -T2 peaks were ranked and
963 the inflection point determined each peak to be top or low-bound. Top-bound peaks were annotated with a
964 corresponding gene and this list of top-bound genes was used as the gene signature. DESeq2 files used
965 in the analysis were pre-ranked. GSEA was performed with the GSEA_4.3.2 desktop application.
966
967 **RNA-FISH with Halo staining**
968 HEK293 cells expressing Halo-tagged ENL transgenes were seeded on poly-L-lysine coated coverslips
969 and grown for 48h in the presence of doxycycline. Live cells were then incubated with 250 nM JF657 Halo
970 ligand for 30 minutes and washed five times in pre-warmed media (5 minutes per wash). Cells were then
971 washed once in PBS + 1% RVC (ribonucleoside vanadyl complex), fixed in 4% PFA + 1% RVC for 10
972 minutes at room temperature, and then washed twice more in PBS 1% RVC. The cells were then
973 permeabilized in 70% ethanol and 1% SDS overnight at 4°C. The next day, the ethanol/SDS solution was
974 removed and the cells were washed twice with 2xSSCT (2xSSC + 0.1% Tween-20) + 1% RVC at room
975 temperature for 5 minutes per wash. Primary probe hybridization mix (2x DSM (dextran sulfate PVSA),
976 50% formamide, 1% SDS, 30 nM primary probe, 1% RVC) was assembled and added dropwise onto a
977 parafilm sheet sitting on top of a damp paper towel in a petri dish. Coverslips were lifted and placed cell-
978 side down onto the hybridization mix drops and denatured at 70°C for 4 minutes. The apparatus was then
979 incubated at 42°C overnight. The following day, the coverslips were transferred back to 24-well plates and
980 washed twice with 2xSCCT + 1% RVC at room temperature, four times with 2xSCCT + 1% RVC at 65°C,
981 and twice more with 2xSCCT + 1% RVC at room temperature. Each wash was 5 minutes. Secondary
982 probe hybridization mix (2x DSM (dextran sulfate PVSA), 50% formamide, 1% SDS, 50 nM dye-conjugated
983 secondary probe, 1% RVC) was assembled and added dropwise onto a parafilm sheet sitting on top of a
984 damp paper towel in a petri dish. Coverslips were lifted and placed cell-side down onto the hybridization
985 mix drops and incubated for 1h at 37°C. Following secondary hybridization, the coverslips were transferred
986 back to 24-well plates and washed four times with 2xSCCT + 1% RVC at 37°C. The coverslips were finally
987 mounted cell side down on slides in DAPI-containing mounting medium. Images were captured on a Zeiss
988 LSM880 confocal microscope.
989
990 Primary probe used: Probes were designed to cover a ~750bp region (19 60mers) of the human *HOXA13*
991 intron. Secondary probes were dye conjugated. For RNA FISH foci intensity measurements, total RNA
992 pixel intensity was measured within each FISH foci boundary and normalized to the total RNA pixel intensity
993 of the corresponding nucleus.
994
995 **Murine hematopoietic stem cell harvest and culture**
996 Whole bone marrow was extracted from euthanized C57BL/6 mice using lower limb centrifugation and
997 subjected to RBC lysis. cKit+ cells were then isolated using the EasySep Mouse CD117 (cKIT) Positive
998 Selection Kit (StemCell). Cells were then stained with Zombie Aqua live/dead dye and cell surface markers
999 (hematopoietic lineage markers, Sca-1, cKit) prior to sorting out $Lin^{-}Sca\text{-}1^{+}cKit^{+}$ cells on a BD FACSAria.
1000 Lineage markers used are CD3, CD19, CD11b, B220, TER119, Gr-1, NK1.1, CD11c, TCRβ, and TCRγ/δ.
1001 LSK cells were cultured for 48h prior to subsequent virus transduction. Cells are cultured in IMDM +
1002 GlutaMAX supplemented with 10% FBS, 100 U/mL penicillin-streptomycin, 20 ng/mL mFlt3L, 20 ng/mL
1003 mIL6, 100 ng/mL mSCF, 20 ng/mL mTPO, 1:1000 0.1M betamercaptoethanol, 1:100 200mM L-glutamine.
1004
1005 **Murine hematopoietic stem cell viral transduction**
1006 For LSK cell infection, the day prior to infection 420 uL of RetroNectin reagent (60 ug/mL) was added to
1007 untreated 24-well cell culture plates and incubated overnight at 4°C. The next day, RetroNectin was

removed and wells were blocked with PBS + 2% BSA for 30 minutes at room temperature. Wells were then washed once with Hank's balanced salt solution (HBSS). After removing the HBSS, desired volume of retrovirus was added to the wells. Plates were centrifuged at 4°C 3000 rpm for 1h. Next, retroviral supernatant was removed and cells were added to the virus-loaded wells with 10 ug/mL polybrene and spinfection was carried out at 37°C 1500rpm for 1.5h. Plates were then incubated overnight. Cell sorting was performed 48-72 hours post-infection.

Colony formation assay

6000 cells were resuspended in 600 uL of IMDM and added to 3mL of MethoCult methylcellulose media supplemented with 10 ng/mL mIL3, 10 ng/mL mIL6, and 20 ng/mL mSCF. 1 mL of the mixture was then added to each well of a 6-well plate (3 replicates total, 2000 cells per replicate). Plates were placed in the incubator and colonies were counted ~1-1.5 weeks after plating. Subsequent re-platings were carried out in the same way.

Bone marrow transplantation and engraftment measurements

LSK cells (CD45.2) were isolated and transduced with ENL transgenes as described above. Transduced LSK were mixed at a 1:3 ratio with RBC-lysed whole bone marrow from a CD45.1/2 mouse (100K LSK: 300K support cells). 400K cells resuspended in 100 uL PBS were injected retro-orbitally to each CD45.1 recipient mouse (B6.SJL-*Ptprc*^{a} *Pepc*^{b}/BoyJ, Jackson Labs #002014). The morning and afternoon prior to injection, CD45.1 recipient mice underwent 2 rounds of lethal irradiation (5.5 Gy per round, 11 Gy total).

Beginning 2 weeks after transplantation, engraftment was measured by peripheral blood staining. Peripheral blood (PB) was harvested by submandibular bleeding into EDTA coated tubes. ~15 uL PB was lysed in 1X RBC lysis buffer for 6 minutes on ice, quenched with FACS buffer (PBS + 2% FBS), and washed once in FACS buffer. Cells were stained with CD45.1 and CD45.2 antibodies (1:200) in FACS buffer for 30 minutes on ice protected from light. Cells were washed once more in FACS buffer and resuspended in FACS buffer + 1:2000 SYTOX blue dead cell stain. Samples were then run on an Attune NxT flow cytometer. Engraftment was measured approximately every 2 weeks for 1 year following transplantation.

Statistics and reproducibility

All experimental observations were confirmed by independent repeat experiments. Experimental data is presented as mean ± standard deviation unless stated otherwise. Statistical significance was calculated by two-tailed, unpaired or paired Student's t-test on two experimental conditions with $P < 0.05$ considered statistically significant unless stated other- wise. The number of replicates and the statistical test used were indicated in the corresponding figure legends. Statistics were performed using GraphPad Prism 10 and RStudio. No data were excluded from the analyses. No statistical methods were used to predetermine sample size. The experiments were not randomized. The investigators were not blinded to allocation during experiments and outcome assessment.